Spectrum Sensing in the Presence of Channel and Tx/Rx Impairments

William Christopher Headley

Dissertation submitted to the Faculty of the

Virginia Polytechnic Institute and State University

in partial fulfillment of the requirements for the degree of

Doctor of Philosophy

in

Electrical Engineering

Jeffrey H. Reed, Chair

Robert W. McGwier

R. Michael Buehrer

Peter M. Athanas

Michael J. Roan

April 29, 2015

Blacksburg, Virginia

Keywords: Spectrum Sensing, Signal Parameter Estimation,

Modulation Classification, Collaborative Sensing

Spectrum Sensing in the Presence of Channel and Tx/Rx Impairments

William Christopher Headley

ABSTRACT

The task of spectrum sensing, defined here to consist of signal detection, signal parameter estimation, and signal identification, is a critically important task in a wide-variety of wireless communication applications. For example, in recent years, government and research initiatives have proposed the idea of communication systems that could gain access to spectrum opportunistically when being unused by primary licensed spectrum users. In order for these opportunistic systems to be realizable, methods by which secondary spectrum users can detect and classify these primary users will be necessary. Furthermore, detection and classification among the secondary users themselves will be important for efficient spectrum usage in these systems. As another example, spectrum sensing is also of critical importance in many military applications. This is due to the inherent expectation that *a priori* information of hostile wireless systems will be minimal or unavailable.

The goal of this dissertation is to provide both insight and solutions in the critical area of spectrum sensing. More specifically, the research contained within this dissertation deals with the development and analysis of spectrum sensing algorithms that address key issues related to channel and radio impairments that are at present underdeveloped in the literature. First, research is presented on a method-of-moments based signal parameter estimation and likelihood-based modulation classification approach for linear digital amplitude-phase modulated signals (PAM, PSK, QAM, ...) in slowly-varying flat-fading channels. Based on this work, research is then presented on a feature-based modulation classification approach which relaxes the requirements of perfect frequency synchronization and knowledge of the phase information of the received signal that the likelihood-based approach requires. Finally, research is presented on the impact that both sensor reliability and sensor correlation information have on collaborative signal detection and intelligent sensor selection.

Dedication

To my parents, my sister, and Jenny, for without their love and support this wouldn't have been possible.

Acknowledgments

First, I would like to thank my advisor Dr. Jeffrey Reed for his guidance and support during my Ph.D. studies. Working with him over the last few years has been a great boon to my skills as a researcher by encouraging me to trust my own abilities, encouraging collaboration with fellow researchers, and providing me with opportunities to enhance my public speaking and research proposal skills. I would also like to thank Dr. Robert W. McGwier for the opportunity to work with the Hume Center at Virginia Tech. Under his guidance, I have been able to apply my knowledge within realistic systems and technologies. Finally, I would like to thank Dr. Claudio da Silva for believing in me as an undergraduate student and taking me on as a graduate student. His guidance in the beginning of my graduate studies was critical to my development as a researcher and as a person.

Secondly, I would like to thank my committee members, Dr. R. Michael Buehrer, Dr. Peter M. Athanas, and Dr. Michael J. Roan for their guidance, time, and support in making this dissertation possible. Special thanks to Dr. R. Michael Buehrer for his kindness, advice, and ribbing during my studies and to Dr. Peter M. Athanas for giving me the opportunity

to work on interesting projects and insights into his area of expertise.

Finally, thanks to all of my friends and colleagues who have supported me during my graduate studies. I would especially like to thank Joseph Gaeddert and Christopher Phelps for being there for me since the beginning. Thanks to Gautham Chavali, Sai Dhiraj, Daniel Jakubisin, Javier Schloemann, Matthew Carrick, Joseph Ernst, and Deirdre Beggs for being great friends and being constant sources of comfort during both the good times and the bad. Also, thanks to Nancy Goad, Hilda Reynolds, and Sonya Rowe for everything they have done for me over the years and for always having their door open for me.

Contents

List of Figures

List of Tables

Chapter 1

Introduction and Motivation

Spectrum sensing encompasses any technique that accomplishes any, or all, of the following signal processing tasks [1]:

- *Detecting* if a signal is present in the observed spectrum
- *Estimating* the parameters of a detected signal of interest, such as
  - center frequency and bandwidth
  - amplitude, phase, and noise power
  - symbol/chip/frame rates
- *Identifying* the signaling format of a detected signal of interest, such as
  - Linear Digital Amplitude-Phase Modulated (LDAPM)
  - Orthogonal Frequency-Division Multiplexed (OFDM)
  - Direct Sequence Spread Spectrum (DSSS)

Each of these signal processing tasks is critical in a wide-variety of commercial and military wireless communication applications.

At present, perhaps the most important commercial wireless communication application for spectrum sensing is *opportunistic*, or *dynamic*, spectrum sharing. More specifically, government and private research initiatives have proposed the idea of wireless communication systems that could access spectrum *opportunistically* when being unused by their primary licensed spectrum users [2],[3]. The primary goal of these proposed opportunistic systems is to address the current shortage of usable spectrum occurring in part due to the inefficient and overly restrictive legacy method of fixed spectrum allocations [4]-[6].

In order for these opportunistic systems to be realizable, fast and reliable interference mitigation techniques must be made available. In other words, spectrum sensing techniques by which the secondary users can *detect*, *estimate*, and *identify* primary users, as well as other secondary users, will be fundamentally important in order to make appropriate spectrum sharing decisions [7]-[9]. Additionally, spectrum sensing has been described as a necessary tool for ensuring spectrum security in opportunistic spectrum sharing applications [10]-[11].

The inherent difficulty in performing spectrum sensing for these applications is that it can be expected that no, or limited, *a priori* knowledge of the signals of interest will be available. Compounding this is the additional fact that the channel, transmitter (Tx), and/or receiver (Rx) impairments can also be expected to be unknown *a priori*. For example, channel impairments such as interference, multi-path, and/or shadowing can distort the signals of interest and thus impact sensing performance [12],[13]. As another example, Tx/Rx impairments such as timing clock offsets/drifts, frequency offsets/drifts, and in-phase/quadrature imbalance may further distort the signal of interest [14],[15].

Given these facts, a critical consideration when developing any spectrum sensing technique lies in the making of valid assumptions on the unknown and known signal, channel, and Tx/Rx parameters for the intended sensing application. For example, prior research in signal parameter estimation and modulation classification typically assumes that the transmitter and receiver are time, frequency, and/or phase synchronous [16]-[21]. However, for opportunistic spectrum sharing scenarios, as well as military applications, these assumptions are typically invalid due to the potentially uncooperative nature of the users in these scenarios.

Additionally, in cooperative spectrum sensing scenarios, in which a network of sensors work collaboratively to determine sensing results, it is typically assumed that each of the sensors in the network are identical and their sensing results are statistically independent of one another. However, given the potentially diverse hardware, software, and time/frequency resources of the sensors in the network, each sensor may have different sensing reliabilities and capabilities that must be considered [22]-[24]. In addition, channel effects such as multipath and shadowing may lead to correlated sensing results among the sensors [25].

1.1 Dissertation Outline and Research Contributions

As just discussed, it is of fundamental importance in the development of spectrum sensing techniques to make valid assumptions on the known and unknown signal, channel, and Tx/Rx parameters for the given spectrum sensing application. With this in mind, the purpose of the work contained within this dissertation is two-fold. First, the goal of this dissertation is to present and quantify spectrum sensing scenarios in which some of the more common signal, channel, and Tx/Rx impairment assumptions typically considered in the literature are relaxed and are therefore more applicable to opportunistic spectrum sharing and military applications. Secondly, and most importantly, the goal of this dissertation is to develop spectrum sensing techniques that address these more realistic sensing scenarios.

In Chapter 2 of this dissertation, a spectrum sensing scenario is presented in which the goal is to estimate the signal and channel parameters, as well as identify the modulation scheme, of an asynchronously received LDAPM signal transmitted in a slowly-varying frequency-flat fading channel. For this sensing scenario, a novel closed-form method-of-moments parameter estimation approach is developed in order to estimate the unknown gain, noise variance, and fractional timing offset of the received signal. The developed estimator requires no *a priori* knowledge of the modulation scheme of the received signal and is invariant to phase information and reasonable frequency offsets. Through simulation it is shown that the developed estimator outperforms the legacy method-of-moments based estimator in which the transmitter and receiver are incorrectly assumed to be synchronous.

Given the developed asynchronous method-of-moments based estimator, Chapter 2 then presents the development of a novel statistical likelihood-based approach to identifying the modulation scheme of the asynchronously received LDAPM signal. The developed classifier is based upon the well-known quasi-Hybrid Likelihood Ratio Test (qHLRT) in which the estimates from the developed method-of-moments based estimator are leveraged in the classifier. Through simulation it is shown that, given an adequate observation interval, the developed classifier's performance approaches that of the optimal synchronous likelihood-based classifier in which all of the received signal parameters are assumed to be known.

A critical assumption in the development of the qHLRT-based modulation classifier is that the transmitter and receiver are perfectly synchronized in frequency. In addition, the developed classifier also requires knowledge (either *a priori* known or through estimation) of the phase of the received signal. In order to remove this dependence on perfect frequency synchronization and complete, or partial, knowledge of the received signal's phase information, Chapter 3 presents the development of a feature-based modulation classification approach which utilizes the statistical measure of kurtosis as the modulation discriminating feature.

More specifically, Chapter 3 first develops a novel closed-form theoretical equation for the kurtosis of asynchronously received LDAPM signals (termed within as the asynchronous kurtosis). Given this closed-form equation, the impact of the SNR, fractional timing delay, and frequency/phase offsets of the received signal on the asynchronous kurtosis is quantified. Next, the developed closed-form equation is utilized in order to developed a novel approach to estimating the kurtosis of the modulation scheme (termed within as the modulation

kurtosis) from estimates of the asynchronous kurtosis and the novel method-of-moments estimator developed in Chapter 2. The performance of this developed modulation kurtosis estimation approach is quantified through both simulation and experimental analysis and is shown to be a valid discriminating feature for modulation classification.

While the focus of Chapters 2 and 3 of this dissertation consider relevant single sensor scenarios for opportunistic spectrum sharing and military applications, it is also important to consider the unique issues that can arise when performing collaborative spectrum sensing for these applications. With this in mind, Chapter 4 presents a collaborative signal detection scenario in which the typically considered assumption of statistically independent and identically performing sensors is relaxed. In other words, it is assumed that the collaborating sensors may be correlated (due to effects such as multi-path fading and/or shadowing, for example) and/or may have different sensing reliabilities (due to proximity to the primary user, different observation intervals, etc.).

Given this collaborative spectrum sensing scenario, a novel collaborative detection algorithm that utilizes knowledge of both the sensor reliability and sensor correlation information is developed and is shown through simulation to outperform algorithms in which one, or neither, of these effects is considered. Given this developed algorithm, a novel approach to intelligent sensor selection is then developed and is shown through simulation to provide more efficient trade-offs between sensing overhead and collaborative sensing performance over random sensor selection.

1.2 Relevant Publications

Journal Papers

- W. C. Headley, R. W. McGwier, and J. H. Reed, "Modulation kurtosis estimation for asynchronous digital amplitude-phase modulated signals," (*to be submitted*).
- S. M. Dudley, W. C. Headley, M. Lichtman, E. Y. Imana, X. Ma, M. Abdelbar, A. Padaki, A. Ullah, M. M. Sohul, T. Yang, J. H. Reed, "Practical issues for spectrum management with cognitive radios," in *Proc. of the IEEE*, vol. 102, no. 3, pp. 242-264, March 2014.
- W. C. Headley, V. G. Chavali, and C. R. C. M. da Silva, "Exploiting radio correlation and reliability information in collaborative spectrum sensing," in *IEEE Commun. Lett.*, vol. 15, no. 8, pp. 825-827, Aug. 2011.
- W. C. Headley and C. R. C. M. da Silva, "Asynchronous classification of digital amplitude-phase modulated signals in flat-fading channels," in *IEEE Trans. Commun.*, vol. 59, no. 1, pp. 7-12, Jan. 2011.

Conference Papers

- M. Lichtman, W. C. Headley, and J. H. Reed, "Automatic modulation classification under IQ imbalance using supervised learning," in *Proc. Military Commun. Conf.*, Nov. 2013, pp. 18-02.
- W. C. Headley, V. G. Chavali, and C. R. C. M. da Silva, "Maximum-likelihood mod-

ulation classification with incomplete channel information," in *Proc. Inf. Theory and Appl. Workshop*, Feb. 2011, pp. 1-4.

White Papers

- A. A. Sohanghpurwala, W. C. Headley, P. Athanas, A. Poetter, D. Mason, and R. Lilley, "Implementation of a dual-mode cognitive radio application on the Harris AppSTAR reconfigurable hardware platform," in *Virginia Tech Wireless Symp.*, Blacksburg, VA, June 2014.

Relevant Master's Publications

- W. C. Headley and C. R. C. M. da Silva, "Asynchronous SNR estimation of PSK/QAM modulated signals in flat-fading channels," in *Proc. IEEE Military Comm. Conf.*, Oct. 2009, pp. 1-5.

- C. R. C. M. da Silva, W. C. Headley, J. D. Reed, and Y. Zhao, "The application of distributed spectrum sensing and available resources maps to cognitive radio systems," in *Proc. Inf. Theory and Appl. Workshop*, Jan. 2008, pp. 53-57.

- W. C. Headley, J. D. Reed, and C. R. C. M. da Silva, "Distributed cyclic spectrum feature-based modulation classification," in *Proc. IEEE Wireless Comm. and Netw. Conf.*, March 2008, pp. 1200-1204.

Chapter 2

Likelihood-based Classification of Asynchronously Received LDAPM Signals in Flat-Fading Channels

As discussed in Section 1, the inherent difficulty in performing spectrum sensing tasks is due primarily to the limited *a priori* knowledge of the signal of interest itself, and any channel, transmitter, and receiver impairments that may exist in the given sensing application. With this in mind, this chapter concerns the development of spectrum sensing approaches under the constraints that the receiver is asynchronous with the signal of interest's transmitter and that the transmission channel is a fading channel with unknown gain and phase effects. In other words, spectrum sensing approaches will be developed under the constraint that the received signal's timing and channel parameters are unknown *a priori*.

More specifically, a novel closed-form statistical signal parameter estimation approach is developed for asynchronously received LDAPM signals given slowly-varying frequency-flat fading channels. To begin this development, first a received signal model is presented in Section 2.2 that incorporates the impact of asynchronous reception in these fading channels. From this model, Section 2.3 presents a novel estimator that uses statistical moments of the received signal in order to estimate the signal's unknown timing and channel parameters. Through simulation, it is shown that this asynchronous estimation approach performs better than a similar moment-based approach in which synchronous reception is assumed.

Given the proposed estimation approach, a novel approach to classifying the modulation scheme of the received LDAPM signal is presented in Section 2.4. More specifically, a likelihood-based modulation classification approach is developed for determining the statistically most-likely modulation scheme based on observations of the received signal. Presented simulation results demonstrate that, given an adequate observation interval, the developed asynchronous classifier performs well compared to the classical optimal synchronous likelihood-based classifier. However, it is shown that this classifier is highly dependent on the phase of the received signal and the assumption that the receiver is perfectly frequency synchronized.

2.1 Acknowledgements

This chapter, in part, is a reprint of the material as it appears in the publication:

- W. C. Headley and C. R. C. M. da Silva, "Asynchronous classification of digital amplitude-phase modulated signals in flat-fading channels," *IEEE Trans. Commun.*, vol. 59, no. 1, pp. 7-12, Jan. 2011.

The dissertation author was the primary author and Dr. Claudio da Silva supervised the research which forms the basis of this chapter.

2.2 The Received Signal Model

A LDAPM signal transmitted at transmitter time ξ can be defined as

$$s(\xi) = A_t \cdot \Re\left\{ \sum_{k=-\infty}^{\infty} S_k f(\xi - kT) e^{j2\pi f_c \xi} \right\}, \tag{2.1}$$

where A_t is the transmitter gain, S_k is the k-th complex-valued modulated data symbol, $f(\xi)$ is the real-valued pulse shaping function, T is the symbol interval (where $1/T$ is the symbol rate), f_c is the center frequency, and $\Re\{\cdot\}$ represents taking the real component of its argument. Without loss of generality, the modulated data symbols S_k and the pulse shaping function $f(\xi)$ are both normalized to have unit average energy (in other words, the gain A_t includes the impact of non-normalization). For this work, the pulse shaping function $f(\xi)$ is chosen to be the root-raised-cosine function given by

$$f(\xi) = \frac{2\beta}{\pi\sqrt{T}} \frac{\cos\left[(1+\beta)\pi\frac{\xi}{T}\right] + \frac{\sin\left[(1-\beta)\pi\frac{\xi}{T}\right]}{4\beta\frac{\xi}{T}}}{\left[1 - \left(4\beta\frac{\xi}{T}\right)^2\right]}, \tag{2.2}$$

where β is the roll-off factor.

Given (2.1), the received signal after transmission through a slowly-varying frequency-flat fading channel can be defined, at transmitter time ξ, as

$$r(\xi) = A_c A_t \cdot \Re\left\{ \sum_{k=-\infty}^{\infty} S_k f(\xi - \xi_c - kT) e^{j(2\pi f_c \xi + \theta_c)} \right\} + n(\xi), \tag{2.3}$$

where $n(\xi)$ is a stationary zero-mean Gaussian random noise process with unknown variance σ^2 and A_c, θ_c, and ξ_c are respectively the unknown gain, phase shift, and time delay introduced by the channel. For the analysis that follows, it is assumed that these unknown channel parameters remain constant during each observation interval.

As previously discussed, a logical constraint for spectrum sensing applications is that the transmitter and receiver clocks are asynchronous. In other words, the transmitter and receiver clocks are offset by a known time constant, here denoted ξ_o. In order to stress these different time references, we use different time indices for the transmitter (ξ) and receiver (t), where $t = \xi - \xi_o$. This model is illustrated through example in Fig. 2.1. It is important to note that this offset between the clock times of the transmitter and receiver is assumed here to not be known by either the transmitter or receiver *a priori*.

For the derivations that follow, it is convenient to write the unknown timing offset due to the combined impact of both the channel delay (ξ_c) and the receiver's clock offset (ξ_o) as a function of the symbol interval T. Therefore, we set $\xi_o - \xi_c = -(l + \epsilon)T$, where l represents the integer number of modulated data symbols offset and ϵ represents the remaining fraction of a modulated data symbol offset ($0 \leq \epsilon < 1$). Given this alternative notation for the timing

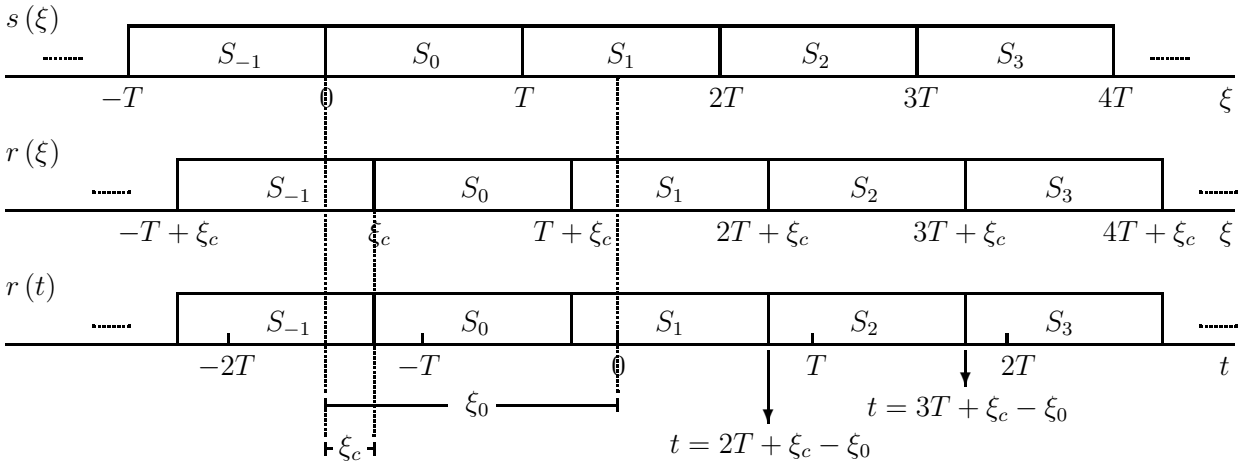

Figure 2.1: Illustration of the transmitted signal $s(\xi)$ and received signal $r(\cdot)$ using the transmitter's (ξ) and receiver's (t) time reference. For ease of presentation, here a rectangular pulse shaping function is used and the channel gain, phase shift, and noise effects are ignored. For this figure, $\xi_c = 0.25T$ and $\xi_o = 1.5T$. *(Figure Credit: Dr. Claudio da Silva.)*

offset, the received signal can be rewritten, using the receiver's time reference t, as

$$r(t) = \alpha \cdot \Re\left\{ \sum_{k=-\infty}^{\infty} S_k f(t-(k+l+\epsilon)T) e^{j(2\pi f_c t+\theta)} \right\} + n(t), \tag{2.4}$$

where $\alpha = A_c A_t$ and θ represents the unknown phase-shift due to the combined impact of the timing offset and the channel. Note that the noise process $n(\cdot)$ is not impacted by the choice of time reference given that it is stationary.

Finally, the signal parameter estimation and modulation classification approaches to be developed in the following are based upon the output of a receiver that consists of the following: a frequency down-converter (from f_c to baseband), a filter matched to the pulse shaping function $f(t)$, and a sampling operation with sampling times $t = (m+\lambda)T$, where m is an arbitrary integer and λ is a real number in the range $[0, 1)$. Given this receiver design,

the received symbols can be shown to be given by

$$\begin{aligned} r_{m,\lambda} &= \int_{-\infty}^{\infty} 2r(\tau)e^{-j2\pi f_c\tau} f((m+\lambda)T-\tau)d\tau \\ &= \alpha e^{j\theta} \sum_{k'=-\infty}^{\infty} S_{m-l-k'} R((k'+\lambda-\epsilon)T) + n_{m,\lambda}, \end{aligned} \tag{2.5}$$

where

$$R(t) = \int_{-\infty}^{\infty} f(\tau)f(t-\tau)d\tau, \tag{2.6}$$

$k' = m-k-l$, and $n_{m,\lambda}$ is a zero-mean complex Gaussian random variable with variance $4\sigma^2$. As expected, when the transmitter and receiver are symbol synchronous (i.e. $\lambda = \epsilon$), (2.5) reduces to

$$r_m = \alpha e^{j\theta} S_{m-l} + n_m. \tag{2.7}$$

The following assumptions about the received signal are used in the development that follows. The modulated data symbols S_k are chosen uniformly and independently from the set of all possible data symbols of the modulation scheme being used by the transmitter. The pulse shape $f(t)$, the symbol interval T, and the carrier frequency f_c are known (unless otherwise noted). All other parameters, namely the amplitude α, phase θ, timing offset $(l+\epsilon)T$, and noise variance σ^2 are modelled as *deterministic unknown variables*.

2.2.1 Impact of Timing Offset on the Received Symbols

Fig. 2.2 provides an example of the impact of the fractional timing offset parameter ϵ, as a function of the roll-off factor β, on the received symbols defined by (2.5). For this figure,

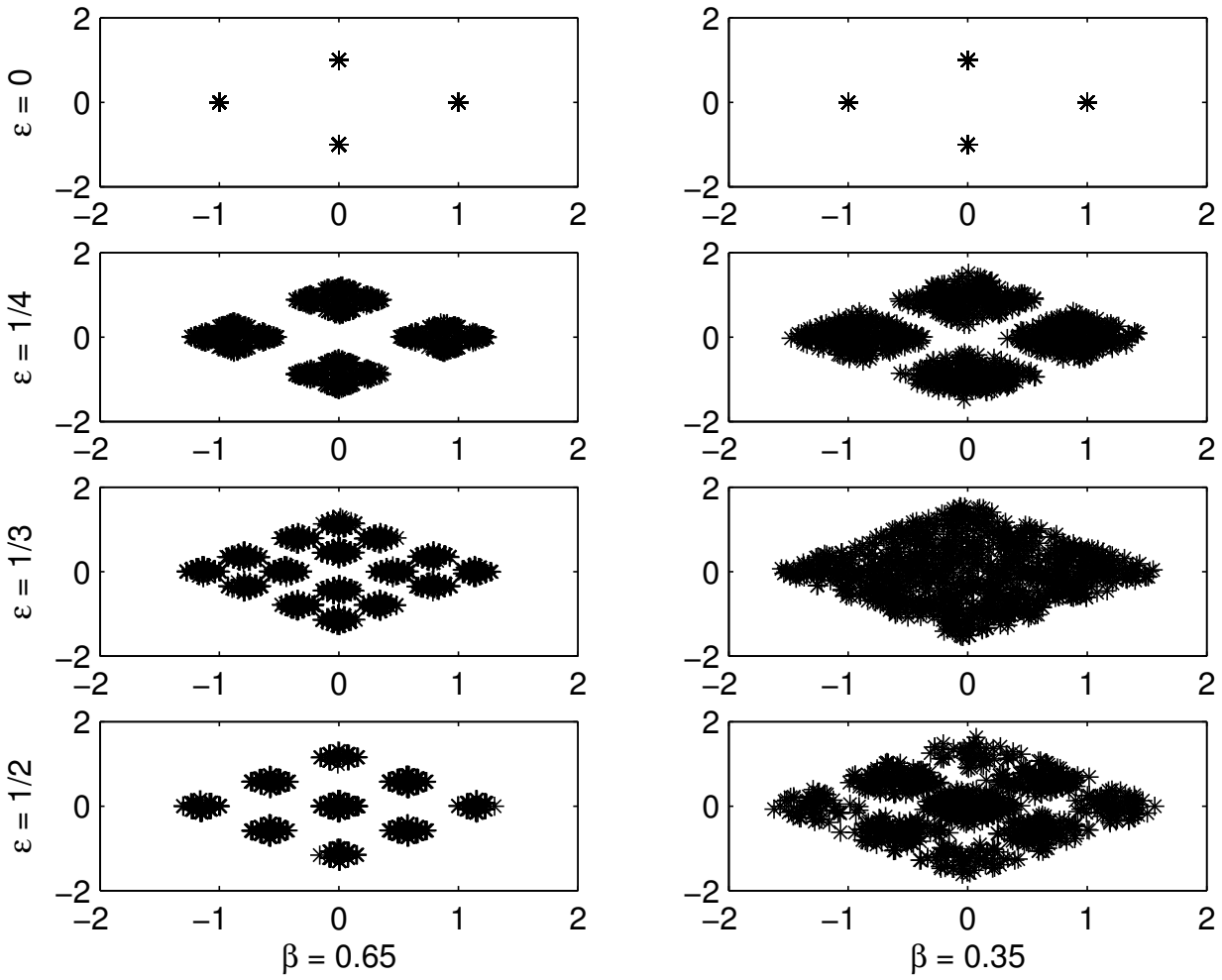

Figure 2.2: The impact of intersymbol-interference on asynchronously received QPSK modulated data symbols as a function of both the fractional timing offset parameter ϵ and the roll-off factor β. (Note that for this figure the channel gain, phase, and noise effects are ignored.)

the modulation scheme is QPSK and the impact of the gain, phase, and noise parameters is ignored.

Two important observations can be made from this figure. First, for a given roll-off factor β, the received QPSK modulated data symbols become increasingly distorted due to inter-symbol interference as ϵ increases, up to a maximum distortion at $\epsilon = 0.5$ (for $\epsilon > 0.5$, the distortion is equivalent to the distortion given $1 - \epsilon$). Secondly, for a given fractional timing offset ϵ, the distortion increases as the roll-off factor β decreases, as expected.

2.3 Signal Parameter Estimation based on the Method-of-Moments

In this section, a novel Method-of-Moments (MoM) based signal parameter estimation approach is defined for estimating the unknown gain α, fractional timing offset ϵ, and noise variance σ^2 from an observed set of received symbols of the form given by (2.5). The MoM is a sub-optimal estimation approach in which the unknown parameters of a random process under observation are estimated through the solution of a system of statistical moment equations derived from the random process' probability density function [26]. As an example of the MoM's prior use in signal parameter estimation, a MoM-based estimator was developed in [20] in order to estimate α, θ, and σ^2 given the assumption of a *synchronous* transmitter and receiver. Additional examples of the use of the MoM for sensing applications can be found in [27] and [28], among many others.

As stated, the unknown received signal parameters α, ϵ, and σ^2 are to be estimated through the solution of a set of statistical moment equations. The first of these moment equations is $\mathrm{E}[|r_{m,\lambda_0}|^2]$, where m is an arbitrarily chosen integer and λ_0 is a real number in the range $[0, 1)$. (It is important to emphasize that the values of m and λ_0 chosen for this moment have no relation to the unknown timing offset parameters l and ϵ.) Substituting (2.5) into this moment equation leads to

$$\begin{aligned}
M_{\lambda_0} &= \mathrm{E}[|r_{m,\lambda_0}|^2] = \mathrm{E}\left[\left|\alpha e^{j\theta}\sum_{k'=-\infty}^{\infty} S_{m-l-k'}R((k'+\lambda-\epsilon)T) + n_{m,\lambda_0}\right|^2\right] \\
&= \mathrm{E}\left[\left|\alpha e^{j\theta}\sum_{k'=-\infty}^{\infty} S_{m-l-k'}R((k'+\lambda-\epsilon)T)\right|^2\right] + \mathrm{E}\left[|n_{m,\lambda_0}|^2\right] \\
&= \alpha^2 \cdot \mathrm{E}\left[\left|\sum_{k'=-\infty}^{\infty} S_{m-l-k'}R((k'+\lambda-\epsilon)T)\right|^2\right] + 4\sigma^2 \\
&= \alpha^2 \cdot \sum_{k'=-\infty}^{\infty} \mathrm{E}[|S_{m-l-k'}|^2]R((k'+\lambda-\epsilon)T)^2 + 4\sigma^2 \\
M_{\lambda_0} &= \alpha^2\psi^{(2)}_{\lambda_0,\epsilon} + 4\sigma^2, \qquad (2.8)
\end{aligned}$$

where the function $\psi^{(2)}_{\lambda_0,\epsilon}$ is given by

$$\psi^{(a)}_{\lambda,\epsilon} = \sum_{k'=-\infty}^{\infty} R((k'+\lambda-\epsilon)T)^a \qquad (2.9)$$

and $\mathrm{E}[|S_{m-l-k'}|^2] = 1$, without loss of generality, due to the prior assumption that the modulation schemes are normalized to unit average energy. It has also been logically assumed in this derivation that the modulated data symbols are independent of the noise.

It is important to note that (2.8) is a function of the unknown parameters α, ϵ, and σ^2, while not being a function of the unknown modulated data symbols, l, or θ. Additionally,

(2.8) is not a function of m, which implies that $\mathrm{E}[|r_{m_1,\lambda_0}|^2] = \mathrm{E}[|r_{m_2,\lambda_0}|^2]$ for all integers m_1 and m_2. For this reason, the subscript m is dropped and the moment is termed M_{λ_0}. Finally, given the root-raised-cosine pulse shaping function defined by (2.2), $\psi^{(2)}_{\lambda_0,\epsilon}$ is shown in Appendix A to be

$$\psi^{(2)}_{\lambda_0,\epsilon} = 1 + \frac{\beta}{4}\left(\cos(2\pi(\lambda_0 - \epsilon)) - 1\right). \tag{2.10}$$

Given (2.10), (2.8) can be rewritten with respect to σ^2 as

$$\sigma^2 = \frac{M_{\lambda_0}}{4} - \frac{\alpha^2}{16}\left(4 + \beta(\cos(2\pi(\lambda_0 - \epsilon)) - 1)\right). \tag{2.11}$$

In order to define the second moment of the proposed MoM-based estimator, a new sampling instant of $(m + \lambda_1)T$ is considered, where again m is an arbitrarily chosen integer and λ_1 is a real number in the range $[0, 1)$, with $\lambda_1 \neq \lambda_0$. Given this new sampling instant, a second equation for σ^2, now as a function of M_{λ_1}, can be found. Setting these two σ^2 equations equal and solving for α^2 leads to

$$\alpha^2 = \frac{4\left(M_{\lambda_0} - M_{\lambda_1}\right)}{\beta\left(\cos(2\pi(\lambda_0 - \epsilon)) - \cos(2\pi(\lambda_1 - \epsilon))\right)}. \tag{2.12}$$

Note that (2.12) is only a function of the unknowns α and ϵ, and is not a function of the unknown σ^2.

The third and final moment for the proposed MoM-based estimator is used to find an equation that is only a function of the unknown fractional timing offset ϵ. Considering a third sampling instant of $(m+\lambda_2)T$, where yet again m is an arbitrarily chosen integer and λ_2 is a real number in the range $[0, 1)$, with $\lambda_2 \neq \lambda_1 \neq \lambda_0$, the moment M_{λ_2} can be determined. Using this third moment, and either of the two previously defined moments (the end result

is the same), a second equation for α^2 can be determined. Setting these two α^2 equations equal and performing some algebraic manipulation leads to

$$Z = \tan(2\pi\epsilon) = \frac{(M_{\lambda_2} - M_{\lambda_1})X_0 + (M_{\lambda_0} - M_{\lambda_2})X_1 + (M_{\lambda_1} - M_{\lambda_0})X_2}{(M_{\lambda_1} - M_{\lambda_2})Y_0 + (M_{\lambda_2} - M_{\lambda_0})Y_1 + (M_{\lambda_0} - M_{\lambda_1})Y_2}, \tag{2.13}$$

where

$$X_i = \cos(2\pi\lambda_i) \tag{2.14}$$

and

$$Y_i = \sin(2\pi\lambda_i). \tag{2.15}$$

Finally, inverting (2.13), and knowing that $\text{atan}(Z)$ has a range of $[-\pi/2, \pi/2]$, ϵ can be found to be given by one of the following three possible values:

$$\epsilon = \left\{ \frac{\text{atan}(Z)}{2\pi}, \frac{\text{atan}(Z)}{2\pi} + \frac{1}{2}, \frac{\text{atan}(Z)}{2\pi} + 1 \right\}. \tag{2.16}$$

The set of equations (2.11), (2.12), and (2.16) can be solved systematically in order to determine the unknown values of α, ϵ, and σ^2 from the moments M_{λ_0}, M_{λ_1}, and M_{λ_2}. More specifically, the following algorithmic approach can be used to determine the values of these unknown parameters:

1. Determine the three moments M_{λ_0}, M_{λ_1}, and M_{λ_2}.

2. Using (2.16), determine the three possible values for ϵ. One of these values can be immediately discarded for falling outside of the defined range $0 \leq \epsilon < 1$.

3. From the remaining two possible values of ϵ, determine the two possible values for α^2 using (2.12). One of these solutions will be negative and can thus be discarded given that by definition α is a real number.

4. Given the unique solutions for ϵ and α, determine σ^2 using (2.11).

In practice however, the true values for the moments M_{λ_0}, M_{λ_1}, and M_{λ_2} are unknown *a priori* and thus must be estimated from the received symbols given by (2.5). These moment estimates are given by

$$\hat{M}_{\lambda_i} = \frac{1}{N_e} \sum_{m=m_i}^{m_i+N_e-1} |r_{m,\lambda_i}|^2, \tag{2.17}$$

where r_{m,λ_i} are the received symbols given a sampling instant of $(m+\lambda_i)T$, N_e is the number of observed received symbols used for estimation, and m_i is an arbitrary integer. Therefore, given that the moments are estimated, the solutions to (2.11), (2.12), and (2.16) will be estimates of the parameters σ^2, α, and ϵ, respectively.

2.3.1 Simulation Results

Figs. 2.3 and 2.4 present simulation results of the performance of the proposed asynchronous MoM-based estimator. For these results, the mean-squared-error (MSE), defined by

$$\text{MSE} = \text{E}\left[|X - \hat{X}|^2\right], \tag{2.18}$$

is used in order to quantify the estimator's performance, where X and $\hat{X}$ are the actual and estimated values, respectively. Each data point in the plots was determined from Monte Carlo analysis of 10,000 trials each, where for each trial, the fractional time delay ϵ is

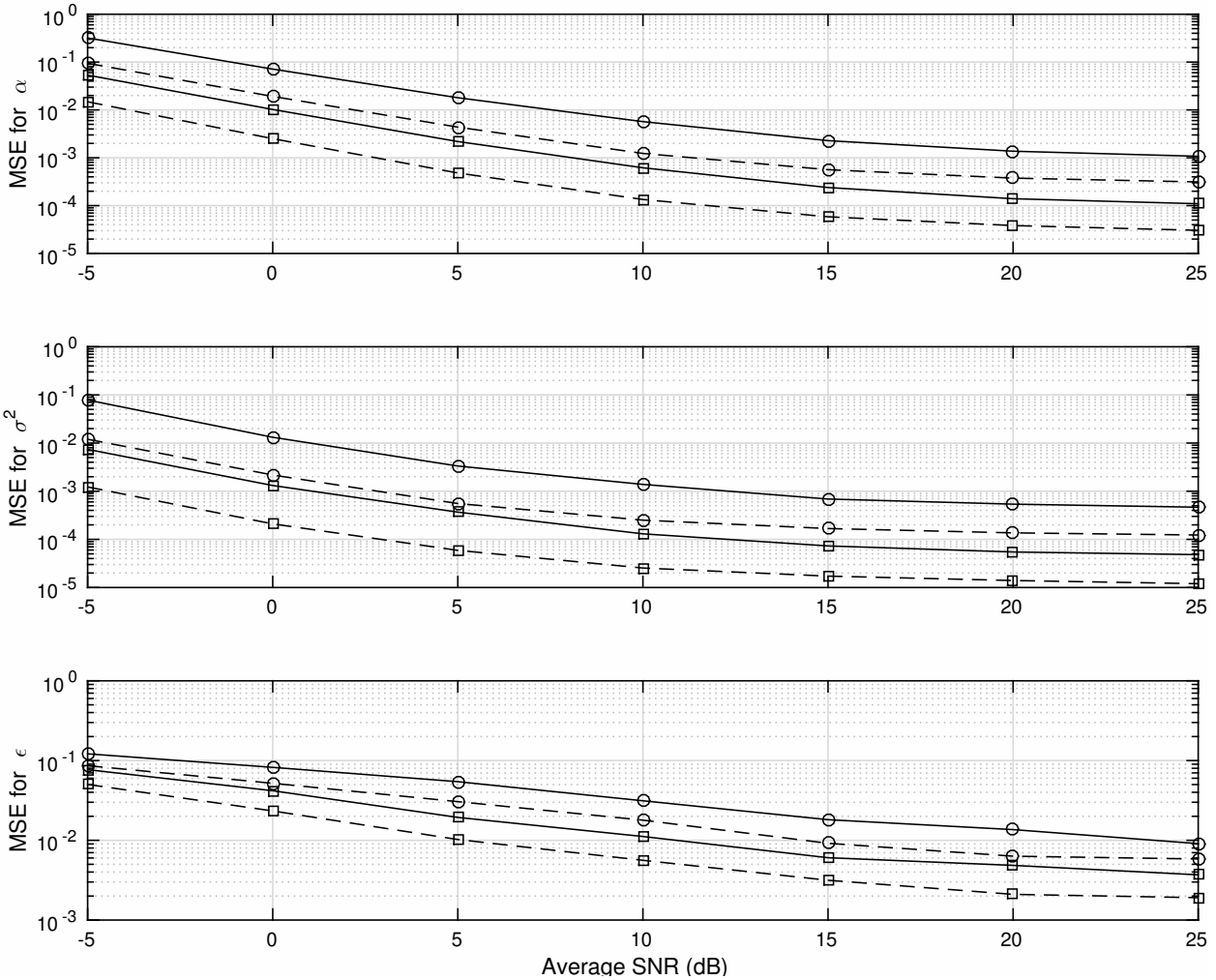

Figure 2.3: MSE of the proposed asynchronous MoM-based estimator for varying N_e and β given a QPSK modulated signal received in a Rayleigh fading channel (circle: $\beta = 0.35$, square: $\beta = 0.75$, solid: $N_e = 1000$, dashed: $N_e = 10000$).

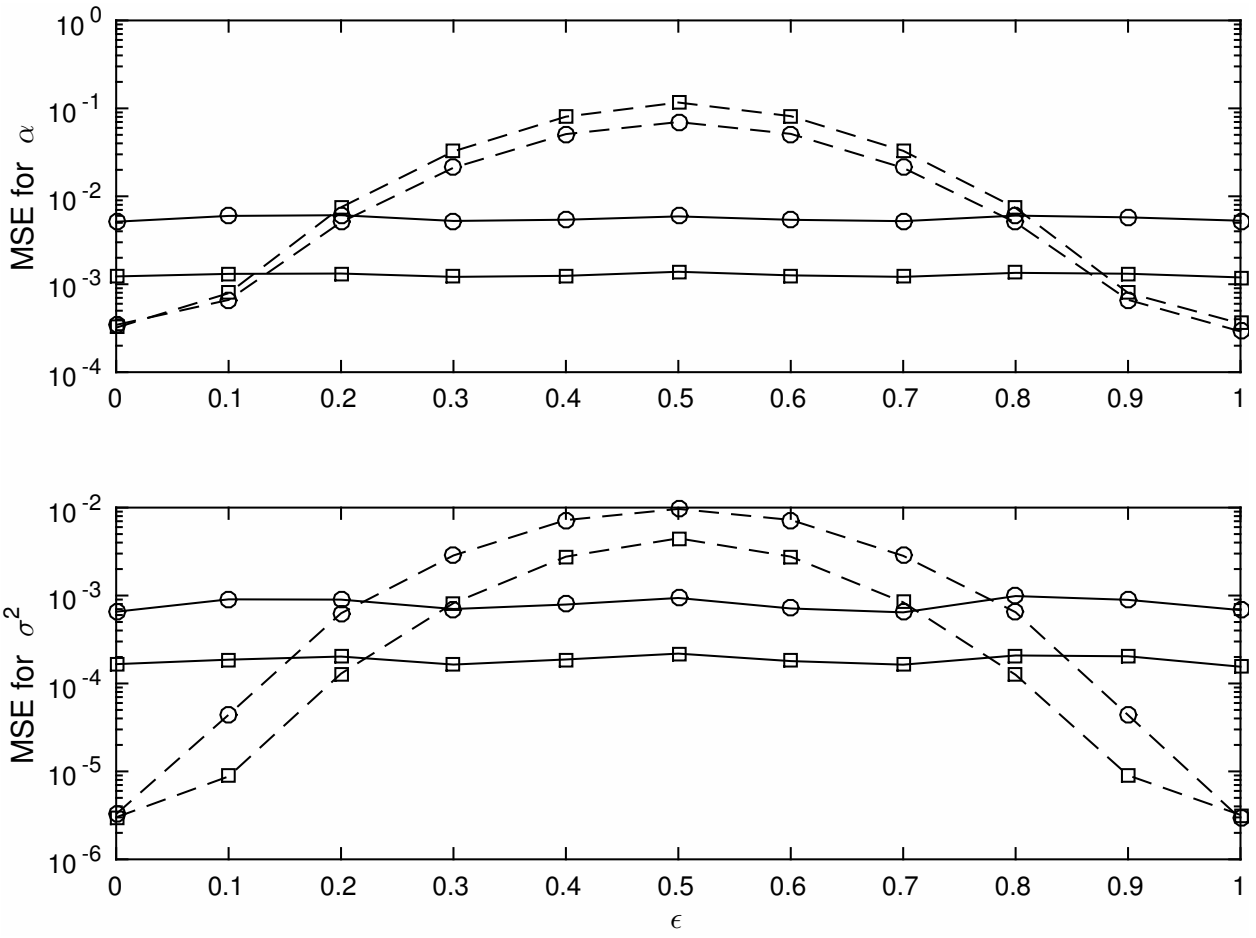

Figure 2.4: MSE of the proposed asynchronous MoM-based estimator (solid line) and the synchronous MOM-based estimator developed in [20] (dashed line) given an average SNR of 10 dB and $N_e = 1000$ (circle: $\beta = 0.35$, square: $\beta = 0.75$).

chosen uniformly in the range $[0, 1)$, unless otherwise noted. Additionally, the set of λ values used in the estimator were chosen to be equally spaced in the range $[0, 1)$ (in other words, $\lambda_{\{0,1,2\}} = \{0, 1/3, 2/3\}$). Finally, a Rayleigh fading channel is assumed in which the amplitude is distributed such that $\mathrm{E}[\alpha^2] = 1$ while the phase θ is assumed to be uniformly distributed in the range $[0, 2\pi)$.

Fig. 2.3 presents the MSE of the estimates of α, ϵ, and σ^2 as a function of the SNR, the number of observed received symbols N_e, and the roll-off factor β, given a QPSK modulated signal received in a Rayleigh fading channel. As expected, as the SNR and/or N_e is increased, the MSE of the estimates decreases. This is due to the fact that an increase in either of these parameters reduces the error of the moments estimated through (2.17), and thus also the estimates derived from these moments. Additionally, it can be observed that the MSE increases for lower roll-off factors. This is due to the fact that the fractional timing offset results in larger inter-symbol interference for lower roll-off factors, as was discussed in Section 2.2.1, leading to an overall reduction in the performance of the estimator.

Fig. 2.4 presents the MSE of the estimates of α and σ^2, as a function of the fractional timing offset ϵ, for the proposed asynchronous estimator and the previously discussed synchronous MoM-based estimator defined in [20], given a QPSK modulated signal received in a Rayleigh fading channel, an average SNR of 10 dB, and $N_e = 1000$. In [20], the estimator for α is given by

$$\alpha^2 = \sqrt{\frac{2M_2^2 - M_4}{2 - \mathrm{E}[|S|^4]}} \tag{2.19}$$

and the estimator for σ^2 is given by

$$\sigma^2 = M_2 - \sqrt{\frac{2M_2^2 - M_4}{2 - \mathrm{E}[|S|^4]}}, \tag{2.20}$$

where $M_2 = \mathrm{E}[|r_m|^2]$, $M_4 = \mathrm{E}[|r_m|^4]$, and r_m is given by (2.7). (Note that this MoM-based estimator is a function of the modulation scheme of the received signal whereas the proposed MoM-based estimator assumes no prior knowledge of the modulation scheme.) As can be observed from the figure, the performance of the synchronous estimator degrades as the fractional timing offset increases to its maximum of 0.5 while the proposed estimation approach is largely invariant to the fractional timing offset, as expected.

2.4 Classification of the Unknown Modulation Scheme

Now that the asynchronous MoM-based estimator for the unknown channel and timing parameters has been developed, this section presents two different approaches to determining the modulation scheme of the asynchronously LDAPM received signal defined by (2.4). In the literature, there are two main approaches to modulation classification, namely likelihood-based approaches and feature-based approaches [29]. For likelihood-based approaches, the conditional probability density function of the received signal is assumed to be completely known, or can be adequately estimated, and from this information the statistically most likely modulation scheme given the observed signal is chosen. For feature-based approaches, modulation dependent features of the received signal are extracted and then used as input to a pattern matching algorithm in order to determine the modulation scheme.

In this section and the following chapter, both a novel likelihood-based modulation classifier and a novel feature-based modulation classifier are presented in order to compare and contrast the benefits and detriments of both approaches. Through simulation, it will be demonstrated under what conditions each approach is valid and in what cases these approaches are best applied. While there are many different types of features that can be used for modulation classification (such as cummulants [30], wavelets [31], cyclostationarity features [32], etc.), in the following chapter the statistical measure of kurtosis is used. The reasoning behind this choice of feature will be discussed in the following.

2.4.1 Likelihood-based Modulation Classification using the qHLRT

Likelihood based classifiers have the key benefit that they are designed to be optimal in the Bayesian sense, in that these classifiers minimize the probability of modulation classification error [33]. More specifically, likelihood-based classifiers are designed as composite hypothesis testing problems in which modulation classification is performed by searching for the maximum *a posteriori* probability $P(\mathcal{H}_i|r(t))$, or equivalently $p(r(t)|\mathcal{H}_i)$ assuming equally likely modulation schemes, where $\{\mathcal{H}_0, \mathcal{H}_1, \ldots\}$ is the set of all possible modulation schemes for the given sensing application.

There are four main approaches to handling unknown parameters in the development of likelihood-based modulation classifiers: the Average Likelihood Ratio Test (ALRT), Generalized Likelihood Ratio Test (GLRT), Hybrid Likelihood Ratio Test (HLRT), and quasi-Hybrid Likelihood Ratio Test (qHLRT). For a detailed discussion of each of these approaches, see

[29]. In this work, a qHLRT-based approach is used in order to develop the *asynchronous* likelihood-based modulation classifier for received LDAPM signals of the form given by (2.4).

For the qHLRT-based approach, the unknown parameters are first estimated through the use of low-complexity estimators that are blind to the modulation scheme of the received signal. These estimates are then used in a modulation classifier developed under the assumption that all parameters are perfectly known. This approach is used for three reasons. First, this approach does not require knowledge of the statistics of the unknown parameters (like the ALRT, for example, which assumes their joint probability density function, conditioned on $\mathcal{H}_i$, is known). Instead, as stated previously, the unknown parameters are modeled as deterministic unknown variables. Secondly, this approach does not require multi-dimensional maximum-likelihood estimation of the unknown parameters, as in the GLRT and HLRT approaches, leading to lower computational complexity and a closed-form solution. Finally, and most importantly, this approach lends itself well to the use of the asynchronous MoM-based estimator developed in Section 2.3.

2.4.2 The qHLRT-based Modulation Classifier

In designing the qHLRT-based modulation classifier, it is first assumed that the receiver has a perfect estimate of the fraction timing offset ϵ. In this case, the vector $\mathbf{r}_\epsilon = [r_{0,\epsilon}, r_{1,\epsilon}, \ldots, r_{N_c,\epsilon}]$, where $r_{m,\epsilon}$ are the synchronously received symbols given by (2.7) and N_c is the number of observed received symbols used for classification, is a set of sufficient statistics for classifying the modulation scheme of the symbols $S_{0-l}, S_{1-l}, \ldots, S_{N_c-l}$ [34] (recall that the integer tim-

ing offset parameter l is assumed to be unknown). Therefore, determining the maximum *a posteriori* probability $p(r(t)|\mathcal{H}_i)$ is equivalent to determining the maximum among $p(\mathbf{r}_\epsilon|\mathcal{H}_i)$.

For an observation length of N_c symbols, there are $L_i^{N_c}$ possible modulated data symbol sequences that can be observed given the i-th modulation scheme, where L_i is the i-th modulation scheme's modulation order. Given that the $r_{m,\epsilon}$ values are assumed independent, the Total Probability Theorem can be used to show that

$$p(\mathbf{r}_\epsilon|\mathcal{H}_i) = \prod_{m=1}^{N_c} \sum_{k=1}^{L_i} p(r_{m,\epsilon}|S_{k,i}, \mathcal{H}_i) P(S_{k,i}|\mathcal{H}_i), \tag{2.21}$$

where $S_{k,i}$ is one of the L_i modulated data symbols of the i-th modulation scheme. Taking the logarithm of $p(\mathbf{r}_\epsilon|\mathcal{H}_i)$, and again using the fact that (2.5) reduces to (2.7) when $\lambda = \epsilon$, leads to the classical optimal likelihood-based modulation classifier developed in [16]:

$$\begin{aligned} \hat{\mathcal{H}} &= \underset{\mathcal{H}_i}{\text{argmax}} \sum_{m=1}^{N_c} \ln \left(\frac{1}{L_i} \sum_{k=1}^{L_i} p(r_{m,\epsilon}|S_{k,i}, \mathcal{H}_i) \right) \\ &= \underset{\mathcal{H}_i}{\text{argmax}} \sum_{m=1}^{N_c} \ln \left(\frac{1}{L_i} \sum_{k=1}^{L_i} e^{-\frac{1}{4\sigma^2}|r_{m,\epsilon} - \alpha e^{j\theta} S_{k,i}|^2} \right), \end{aligned} \tag{2.22}$$

where $P(S_{k,i}|\mathcal{H}_i) = 1/L_i$ given equally likely modulated data symbols.

As stated previously, the value of l (the integer number of modulated data symbols offset) is irrelevant for the purposes of modulation classification. In other words, the modulation classifier's performance is the same if the symbols $S_0, S_1, \ldots, S_9$ or $S_{55}, S_{56}, \ldots, S_{64}$ are observed (assuming that the channel and timing parameters remain constant). However, the modulation classifier is dependent on the fractional timing offset ϵ. Also, note that the classifier is a function of the phase θ and the number of observed received symbols N_c.

Finally, it is important to recall that α, ϵ, θ, and σ^2 are assumed to be *deterministic unknown variables*. Therefore, the qHLRT-based approach dictates that these parameters are replaced by their estimates (denoted by $\hat{}$) in the developed modulation classifier. This leads to the final form of

$$\hat{\mathcal{H}} = \underset{\mathcal{H}_i}{\operatorname{argmax}} \sum_{m=1}^{N_c} \ln \left\{ \frac{1}{L_i} \sum_{k=1}^{L_i} e^{-\frac{1}{4\sigma^2}|r_{m,\hat{\epsilon}} - \alpha e^{j\theta} S_{k,i}|^2} \right\} \tag{2.23}$$

for the *asynchronous* qHLRT-based modulation classification algorithm, where $r_{m,\hat{\epsilon}}$ is given by (2.5) assuming a sampling instant of $(m+\hat{\epsilon})T$.

2.4.3 Simulation Results

A block diagram of the developed asynchronous qHLRT-based modulation classifier is presented in Fig. 2.5. As shown, the classifier first estimates α, ϵ, and σ^2 using the asynchronous MoM-based estimator previously defined in Section 2.3. Using the estimated fractional timing offset $\hat{\epsilon}$, a delayed version of the demodulated received signal is sampled at the sampling instants $(m+\hat{\epsilon})T$ to provide the outputs $r_{m,\hat{\epsilon}}$. These outputs are then used to estimate θ and to classify the modulation scheme of the received signal.

For the simulation results that follow, the unknown phase θ is estimated using a MoM-based algorithm known as the M-power phase synchronizer [20], [35]. This estimator uses estimates of the M-th moment of the received symbols $r_{m,\hat{\epsilon}}$ in order to estimate the phase, where M depends on the modulation scheme of the received signal. For example, for PSK

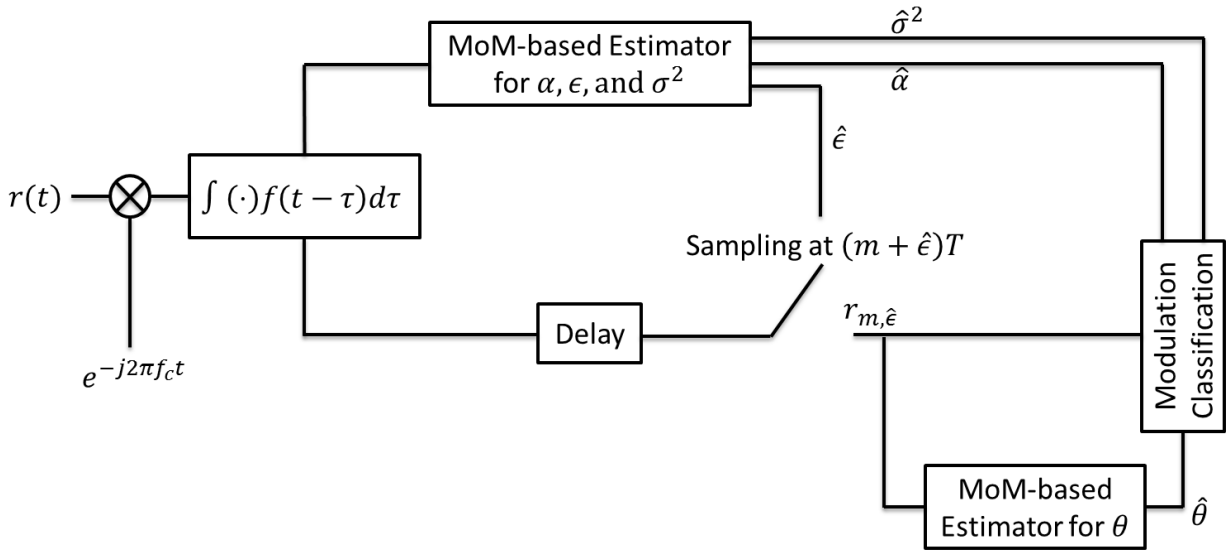

Figure 2.5: Block diagram of the developed asynchronous qHLRT-based modulation classifier.

modulation schemes, the phase estimator is given by

$$\hat{\theta}_{\text{M-PSK}} = \frac{1}{M} \arg \left\{ \sum_{m=1}^{N_c} r_{m,\hat{\epsilon}}^{M} \right\}, \tag{2.24}$$

where M is the order of the PSK modulation scheme under test. For QAM modulation schemes, the phase estimator is given by

$$\hat{\theta}_{\text{QAM}} = \frac{1}{4} \arg \left\{ \sum_{m=1}^{N_c} r_{m,\hat{\epsilon}}^{4} \right\}. \tag{2.25}$$

Note that while this estimator works well for square QAM, it performs poorly for circular and cross QAM [36]. Additionally, a phase estimate must be determined for each of the possible modulation schemes of the received signal.

Figs. 2.6 and 2.7 present simulation results of the performance of the proposed asynchronous qHLRT-based modulation classifier. For these results, the average probability of

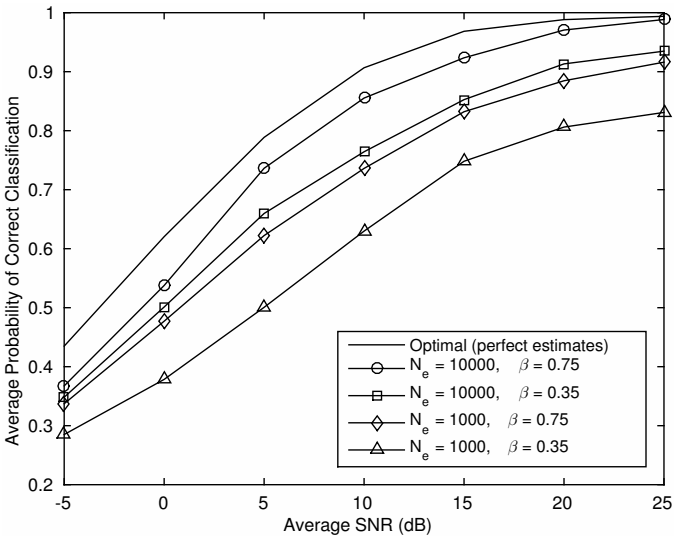

Figure 2.6: Average probability of correct classification of the proposed asynchronous qHLRT-based modulation classifier given a Rayleigh fading channel and $N_c = 500$. The performance of the optimal likelihood-based classifier developed in [16] is also provided for comparison.

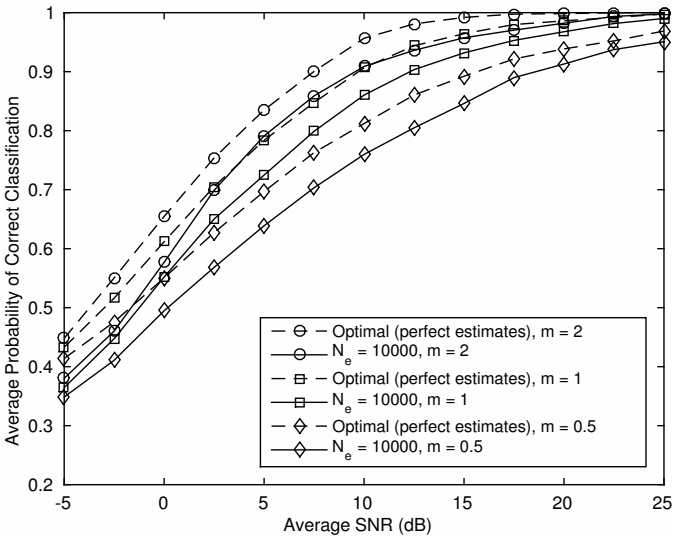

Figure 2.7: Average probability of correct classification of the proposed asynchronous qHLRT-based modulation classifier given a Nakagami fading channel, $N_c = 500$, and $\beta = 0.75$. The performance of the optimal likelihood-based classifier developed in [16] is also provided for comparison.

correct classification, defined by

$$\tilde{P}_{\text{Class}} = \frac{1}{c}\sum_{i=1}^{c}\frac{N_{\text{Correct},i}}{N_{\text{Trials},i}}, \tag{2.26}$$

is used in order to quantify the classifier's performance, where c is the number of possible modulation schemes, N_{Trials} is the total number of Monte Carlo trails, and N_{Correct} is the number of correct classifications found during these trials. More specifically, each of the data points in the plots were determined from Monte Carlo analysis by running enough trials to ensure $N_{\text{Correct}} = 1000$ for each possible modulation scheme. The modulation schemes considered here are BPSK, QPSK, 8-PSK, 16-QAM, and 64-QAM and the set of λ values used by the proposed asynchronous MoM-based estimator are given by $\lambda_{\{0,1,2\}} = \{0, 1/3, 2/3\}$.

In Fig. 2.6, a Rayleigh fading channel is assumed in which the amplitude is distributed such that $\mathrm{E}[\alpha^2] = 1$ and the phase θ is assumed to be uniformly distributed in the range $[0, 2\pi)$. From this figure, the effects of the reliability of the estimates $\hat{\alpha}$, $\hat{\theta}$, $\hat{\epsilon}$, and $\hat{\sigma}^2$ on the performance of the proposed asynchronous qHLRT-based modulation classifier can be observed. More specifically, as the reliability of the estimates improves, be it through higher values of N_{e}, β, and/or SNR, as discussed in Section 2.3.1, the performance of the modulation classifier improves, as expected. Additionally, it can be seen that the classifier's performance closely approaches that of the *optimal* classifier with perfect channel and timing knowledge (developed in [16]) for an adequate estimation interval.

In Fig. 2.7, a Nakagami fading channel is assumed in which the amplitude is again distributed such that $\mathrm{E}[\alpha^2] = 1$ and the phase θ is again assumed to be uniformly distributed

in the range $[0, 2\pi)$. More specifically, this figure presents the performance of the proposed asynchronous qHLRT-based modulation classifier for different values of the Nakagami shape factor m. As can be seen, the performance of the modulation classifier improves as m increases. This is due to the fact that the Nakagami probability density function has smaller variance for larger values of m [37]. Additionally, it is worth noting that, for $m = 1$, the modulation classifier's performance is equivalent to the performance due to Rayleigh fading, as expected.

2.4.3.1 Impact of Roll-off Factor Mismatch

It can be expected that in practice the roll-off factor of the transmitter's pulse shaping filter may not be perfectly known. Therefore, in Fig. 2.8 the performance of the proposed qHLRT-based modulation classifier is presented for the case in which the roll-off factors of the pulse shaping filters at the receiver and the transmitter are mismatched. More specifically, it is assumed that the roll-off factor of the matched filter used by the modulation classifier is a uniformly distributed random variable in the range $[\beta - X, \beta + X]$, where β is the roll-off factor of the transmitter's pulse shaping filter. As can be expected, there is a performance hit as the range of the mismatch increases. However, even for $X = 0.1$ the decrease in the average probability of correct classification is only approximately 7%.

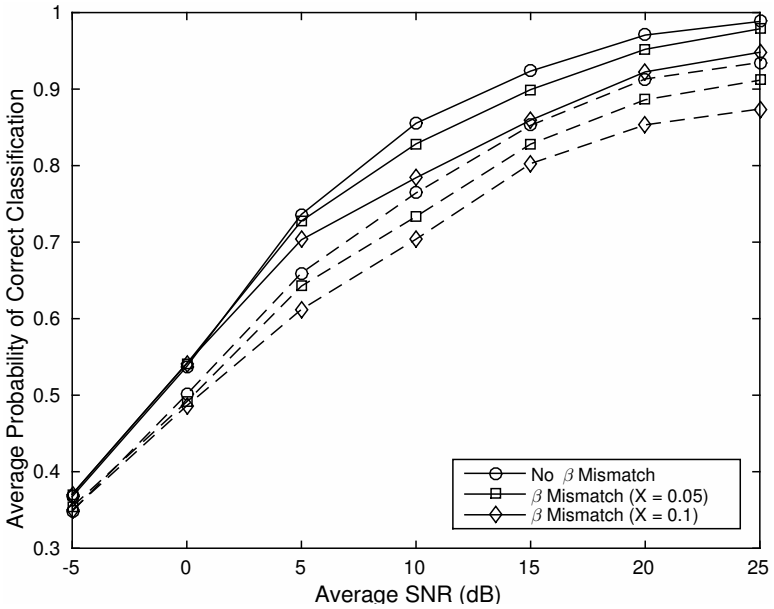

Figure 2.8: Average probability of correct classification of the proposed asynchronous qHLRT-based modulation classifier given roll-off factor mismatch for a Rayleigh fading channel, $N_{\mathrm{e}} = 10000$, and $N_c = 500$ (solid: $\beta = 0.75$, dashed: $\beta = 0.35$).

2.5 Summary

In this chapter, a novel statistical approach to signal parameter estimation and modulation classification was developed under the constraint that the channel and timing impairments on the received signal of interest are unknown *a priori*. First, a novel closed-form asynchronous method-of-moments based estimator was developed in order to estimate these impairments, and through simulation, this estimator was shown to outperform a similar approach in which synchronization is assumed. From this estimator, a likelihood-based classification approach was propose and through simulation results was shown to perform comparatively well to the optimal likelihood-based classifier, in which the impairments are assumed perfectly known, given an adequate observation interval.

Chapter 3

Feature-based Classification of Asynchronously Received LDAPM Signals in Flat-Fading Channels

In the previous chapter, simulation results showed that the developed asynchronous qHLRT-based modulation classifier has performance comparable to that of the classical optimal likelihood-based modulation classifier, given adequate estimates of the unknown channel and timing parameters. However, a couple of key downsides are apparent in the proposed modulation classifier, which apply to other likelihood-based modulation classifiers in general. First, as can be observed from (2.23), the proposed modulation classification algorithm includes a summation over the total number of observed received symbols (N_c), as well as the total number of possible modulated data symbols (L_i), for each of the potential modulation schemes of the received signal for the given sensing application. This leads to high computational complexity as the number of possible modulation schemes, the order

of those modulation schemes, and the number of observed received symbols increases [29]. Secondly, the complete set of possible modulation schemes must be known *a priori*.

For feature-based modulation classification approaches, modulation dependent features of the received signal are extracted and then used as input to a pattern matching algorithm in order to determine the modulation scheme. These approaches are typically much less computationally intensive than likelihood-based approaches, but have no inherent guarantees of optimality. Additionally, while likelihood-based classifiers are theoretically well-defined, the features and pattern matching algorithms chosen for feature-based classifiers are typically determined in an ad-hoc manner. In other words, appropriate features and pattern matching algorithms are typically determined through trial and error and are application dependent.

Commonly, the chosen features are statistical measurements of the signal of interest. For example, prior works have demonstrated that the statistical measurement of kurtosis is a signal feature that can be utilized in a wide variety of spectrum sensing applications, such as modulation classification (see [38]-[44], among many others). This is due to the fact that the kurtosis has a few key benefits which makes it advantageous in these applications. One such benefit is the fact that the kurtosis is simply a function of statistical moments and therefore does not require a large amount of computational resources. Another key benefit is that the kurtosis is not a function of phase information, a fact that will be exploited and discussed in greater detail in the following.

In prior modulation classification works, the kurtosis of the received signal of interest is typically presented under the assumption that the impact of the transmit channel is perfectly

known and/or that the transmitter and receiver are synchronized. In [44], for example, the impact of the channel on the kurtosis is considered, but the impact of timing offset is ignored. While in [45], the impact of the timing offset on the kurtosis is considered but the impact of the channel is ignored.

In the following, the theoretical kurtosis of the asynchronously received symbols given by (2.5) is presented, in which the impact of both channel and timing impairments is considered. From this derivation of the kurtosis, a novel estimation approach is proposed that utilizes the asynchronous MoM-based estimator developed in Section 2.3 in order to estimate the so-called "modulation kurtosis" of the received signal. It will then be shown through both simulation and experimental analysis that this estimate of the modulation kurtosis can be utilized for the purposes of modulation classification.

3.1 Acknowledgements

This chapter, in part, is a reprint of the material as it appears in the publication:

- W. C. Headley, R. W. McGwier, and J. H. Reed, "Modulation kurtosis estimation for asynchronous digital amplitude-phase modulated signals," (submitted to *IEEE Wireless Lett.*, Mar. 2015).

The dissertation author was the primary author and Prof. Jeffrey Reed and Prof. Robert McGwier supervised the research which forms the basis of this chapter.

3.2 The Modulation Kurtosis

The kurtosis of a random variable is a statistical measurement of the "peakedness" of its probability density function around its mean, typically compared with respect to the standard normal distribution. While there exists a commonly agreed upon definition of the kurtosis for real-valued random variables [33], there is no one definitive equation for the kurtosis of complex-valued random variables [46]. For this work however, the kurtosis of a complex-valued zero-mean random variable X is defined as [45]

$$\kappa_X = \frac{\mathrm{E}[|X|^4] - 2\mathrm{E}[|X|^2]^2 - |\mathrm{E}[X^2]|^2}{\sigma_X^4}, \tag{3.1}$$

where σ_X represents the standard deviation of X. This definition of the kurtosis is typically referred to as the *excess kurtosis*, due to the fact that it is normalized to yield $\kappa = 0$ for the complex standard normal distribution.

As previously discussed, for any LDAPM signal, the data to be transmitted is mapped onto one of the M complex-valued symbols that make up the symbol set of the transmitter's chosen modulation scheme ($[s_1, s_2, \ldots, s_M]$). Here, a transmitted modulated data symbol is represented by the complex-valued discrete random variable

$$S = s_{\Re} + j s_{\Im}, \tag{3.2}$$

where $s_{\Re}$ and $s_{\Im}$ are respectively the real and imaginary components of the random variable. Assuming that the values of S are chosen independently and uniformly from the chosen symbol set (e.g. through proper source coding of the data at the transmitter [37]), a general

equation for the kurtosis for S, termed here the *modulation kurtosis* (κ_{MOD}), can be found through (3.1) to be given by (assuming the symbols are normalized such that $\text{E}[|S|^2 = 1)$

$$\kappa_{\text{MOD}} = \kappa_S = \text{E}[s_{\Re}^4] + \text{E}[s_{\Im}^4] + 2(\text{E}[s_{\Re}^2 s_{\Im}^2] - \text{E}[s_{\Re}^2]\text{E}[s_{\Im}^2]) - 3(\text{E}[s_{\Re}^2]^2 + \text{E}[s_{\Im}^2]^2). \tag{3.3}$$

Table 3.1 presents the key terms of (3.3), and the resulting modulation kurtosis, for some typical modulation schemes. As can be observed from this table, the modulation kurtosis lends itself well to modulation classification applications. For example, the modulation kurtosis can be used to distinguish between the modulation schemes PAM, PSK, and QAM. Additionally, the modulation kurtosis can be used to determine the order of the PAM and QAM modulation schemes. However, it is important to note that the modulation kurtosis alone can not be used to classify between the modulation orders of PSK. This is again due to the fact that phase information is ignored in the calculation of the kurtosis.

Table 3.1: Modulation Kurtosis of a few Common Modulation Schemes

	Modulation Scheme				
	BPSK	QPSK	M-PSK (M>4)	M-QAM (M EVEN)	M-PAM
$\text{E}[s_{\Re}^2]$	1	0.5	0.5	0.5	1
$\text{E}[s_{\Im}^2]$	0	0.5	0.5	0.5	0
$\text{E}[s_{\Re}^2 s_{\Im}^2]$	0	0	0.125	0.25	0
$\text{E}[s_{\Re}^4]$	1	0.5	0.375	$\frac{3}{4} - \frac{3}{10}\left(\frac{M+1}{M-1}\right)$	$\frac{3}{5}\left(\frac{3M^2-7}{M^2-1}\right)$
$\text{E}[s_{\Im}^4]$	0	0.5	0.375	$\frac{3}{4} - \frac{3}{10}\left(\frac{M+1}{M-1}\right)$	0
κ_{MOD}	-2	-1	-1	$-\frac{3}{5}\left(\frac{M+1}{M-1}\right)$	$-\frac{6}{5}\left(\frac{M^2+1}{M^2-1}\right)$

3.3 The Kurtosis of the Received LDAPM Symbols

Now that the concept of the modulation kurtosis has been established, it is important to quantify the impact that the timing and channel effects have on the kurtosis of the modulated data symbols at the receiver. From the received LDAPM symbols given by (2.5), the kurtosis of these received symbols is found in Appendix B to be given by

$$\kappa_r = \kappa_{\text{MOD}} \frac{\alpha^4 \psi^{(4)}_{\lambda,\epsilon}}{(\alpha^2 \psi^{(2)}_{\lambda,\epsilon} + 4\sigma^2)^2}, \tag{3.4}$$

where κ_{MOD} is the modulation kurtosis given by (3.3) and $\psi^{(2)}_{\lambda,\epsilon}$ and $\psi^{(4)}_{\lambda,\epsilon}$ are derived for the root-raised-cosine pulse shaping function in Appendix A. Note that the integer number of symbols offset and the unknown phase θ have no impact on the kurtosis of the received symbols.

As can be observed from (3.4), the modulation kurtosis is impacted by the unknown channel gain α, unknown fractional timing offset ϵ, and the unknown noise variance $4\sigma^2$. In the following, a few important observations are made on the impact that these impairments have on the modulation kurtosis.

3.3.1 Impact of the SNR on the Kurtosis

Under the assumption that the transmitter and receiver are synchronized (i.e. $\lambda = \epsilon$), $\psi^{(2)}_{\lambda,\epsilon} = \psi^{(4)}_{\lambda,\epsilon} = 1$, which leads to the simplified expression

$$\kappa_r = \kappa_{\text{MOD}} \frac{\alpha^4}{(\alpha^2 + 4\sigma^2)^2}. \tag{3.5}$$

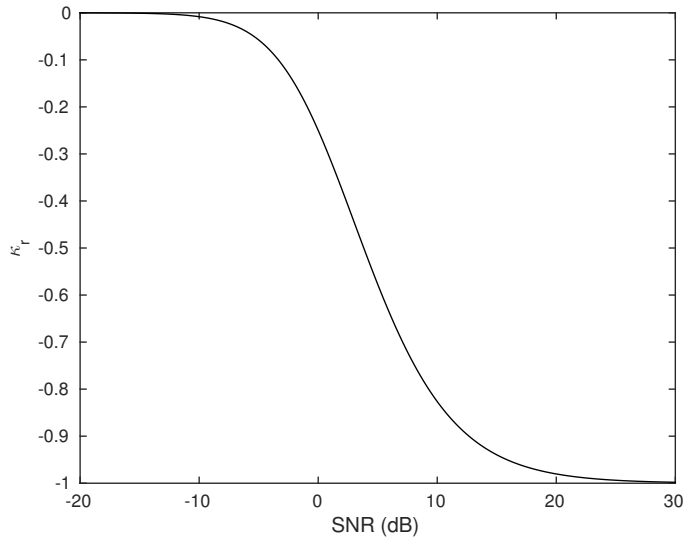

Figure 3.1: Impact of the SNR on the modulation kurtosis assumed MPSK modulation ($M > 4$). Here, the impact of the fractional time delay ϵ is ignored.

Fig. 3.1 plots (3.5) as a function of SNR for a MPSK ($M > 4$) modulated signal. From this figure, it can be observed that as the instantaneous SNR, given here by $\alpha^2/(4\sigma^2)$, increases, the kurtosis of the received symbols approaches the modulation kurtosis of M-PSK (-1), as expected. However, when the SNR decreases, the kurtosis approaches 0, the kurtosis for a purely Gaussian complex random variable.

3.3.2 Impact of Timing Offset on the Kurtosis

Assuming a noise-less channel but non-synchronous receiver with $\alpha = 1$, the kurtosis given by (3.5) simplifies to

$$\kappa_r = \kappa_{\text{MOD}} \frac{\psi^{(4)}_{\lambda,\epsilon}}{\psi^{(2)^2}_{\lambda,\epsilon}}. \tag{3.6}$$

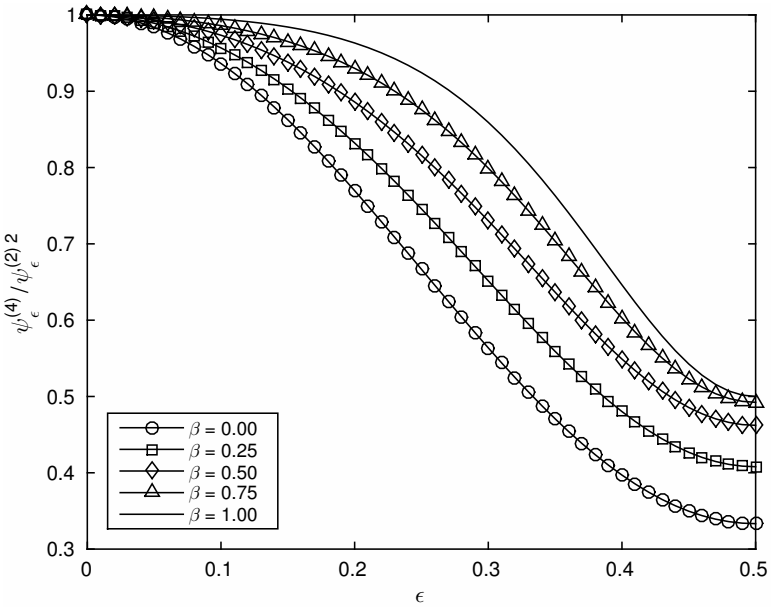

Figure 3.2: Impact of the roll-off factor β and the fractional time delay ϵ on the modulation kurtosis. Here, channel gain and noise effects are ignored. These theoretical results match the results obtained through simulation in [45].

Fig. 3.2 plots the term $\psi_{\lambda,\epsilon}^{(4)}/\psi_{\lambda,\epsilon}^{(2)^2}$ as a function of the roll-off factor β and the fractional timing offset ϵ (assuming here that $\lambda = 0$). A couple of observations can be made from this figure. First, the smaller the roll-off factor β, the bigger the impact of the fractional timing offset on the kurtosis. This is again due to the fact that the inter-symbol interference increases as the roll-off factor decreases. Secondly, it can be observed that the largest impact on the kurtosis is for $\beta = 0$ and $\epsilon = 0.5$ (the worst possible timing offset). For these values, a minimum of 1/3 of the modulation kurtosis is reached. These observations match the results found through simulation in [45].

3.3.3 Impact of Frequency Offset on the Kurtosis

If the receiver previously defined in Section 2.2 has a frequency down-conversion stage that is not perfectly matched to the received signal's center frequency f_c, the received symbols can be shown to be given by

$$\begin{aligned} r_{m,\lambda} &= \int_{-\infty}^{\infty} 2r(\tau)e^{-j2\pi(f_c+f_o)\tau} f((m+\lambda)T-\tau)d\tau \\ &= \alpha e^{j(\theta-\theta_m)} \sum_{k'=-\infty}^{\infty} S_{m-l-k'} R((k'+\lambda-\epsilon)T) + n_m, \end{aligned} \tag{3.7}$$

where f_o is the frequency offset and θ_m is the resulting phase-shift due to this offset (assuming $f_o << 1/T$). More specifically, the received symbols are impacted by a continuous phase rotation (hence the subscript m on the phase term).

For modulation schemes that are symmetric in both their real and imaginary components (such as PSK and QAM) the modulation kurtosis is unaffected by this phase rotation. However, for modulation schemes that are not symmetric (such as PAM) the value of the modulation kurtosis is impacted by the phase rotation. For example, the modulation kurtosis of BPSK becomes -1 (the modulation kurtosis for M-PSK). Additionally, the modulation kurtosis for PAM becomes $\frac{1}{5}\left(\frac{M^2+11}{M^2-1}\right)$. Note that this modulation kurtosis for PAM can still be used for the purposes of classifying its modulation type and modulation order.

3.3.4 Simulation Results

Given the asynchronous kurtosis defined by (3.4), and the asynchronous MoM-based estimator developed in Section 2.3 in order to estimate the unknowns α, ϵ, and σ^2, the modulation kurtosis of the received signal can be estimated through manipulation of (3.4) to give

$$\hat{\kappa}_{\text{MOD}} = \hat{\kappa}_r \frac{(\hat{\alpha}^2 \hat{\psi}^{(2)}_{\lambda,\epsilon} + 4\hat{\sigma}^2)^2}{\hat{\alpha}^4 \hat{\psi}^{(4)}_{\lambda,\epsilon}}. \tag{3.8}$$

Figs. 3.3 and 3.4 present simulation results of the performance of this proposed approach to modulation kurtosis estimation. For these results, the normalized mean-squared-error (NMSE), defined by

$$\text{NMSE} = \frac{\text{E}\left[|\kappa_{\text{MOD}} - \hat{\kappa}_{\text{MOD}}|^2\right]}{\text{E}\left[|\kappa_{\text{MOD}}|^2\right]}, \tag{3.9}$$

is used in order to quantify the estimator's performance, where κ_{MOD} and $\hat{\kappa}_{\text{MOD}}$ are the actual and estimated values of the modulation kurtosis, respectively. Each data point in the plots was determined from Monte Carlo analysis of 1000 trials each, where for each trial the fractional time delay ϵ is chosen uniformly in the range [0,1). Again, the set of λ values $\{0, 1/3, 2/3\}$ are used by the developed MoM-based estimator for estimating the unknown channel and timing parameters. Finally, the unknown amplitude α is assumed to be due to a Rayleigh fading channel and is distributed such that $\text{E}[\alpha^2] = 1$.

Fig. 3.3 presents the NMSE of the modulation kurtosis estimate as a function of the number of observed received symbols N_e, the roll-off factor β of the root-raised-cosine pulse shape, and the SNR of the received signal. A few important observations can be made from this figure. First, as expected, the performance of the estimator increases as the SNR and/or

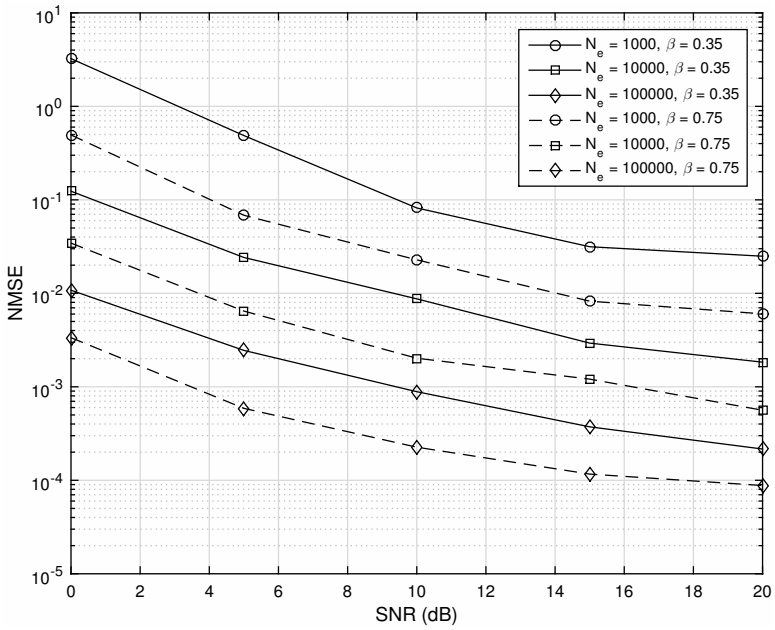

Figure 3.3: NMSE of the proposed modulation kurtosis estimator for varying N_e and β given a QPSK modulated signal received in a Rayleigh fading channel.

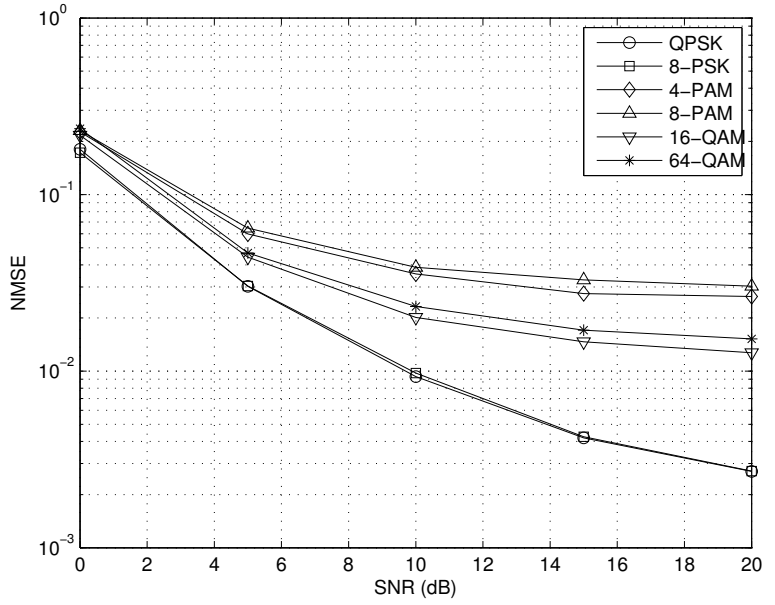

Figure 3.4: NMSE of the proposed modulation kurtosis estimator for varying modulation schemes given $\beta = 0.35$, $N_e = 10000$, and a Rayleigh fading channel.

the observation length increases. Secondly, the performance of the estimator increases as the roll-off factor increases, due to decreased inter-symbol interference.

Fig. 3.4 presents the NMSE of the modulation kurtosis estimate as a function of the SNR and the modulation scheme of the received signal. From this figure, it can be observed that the NMSE is lowest for the PSK modulation schemes and is not a function of their modulation order. This is due to the fact that, for PSK modulations, the difference among the modulated data symbols is in the phase only, and as discussed previously, the kurtosis is not a function of phase information.

From this figure it can also be observed that, for QAM and PAM modulation schemes, the NMSE increases as the modulation order increases. Additionally, the performance given QAM is better than the performance given PAM. This is due to the fact that these modulation schemes have symbols that differ in amplitude. More specifically, as the modulation order of these schemes increases, their fourth absolute moment, defined by $\mathrm{E}[|S|^4]$, increases. This leads to larger variance in the estimates and thus decreases their performance.

3.3.4.1 Modulation Classification using the Modulation Kurtosis Estimator

Fig. 3.5 presents the performance of a feature-based modulation classifier that uses estimates of the modulation kurtosis given by (3.8) in order to perform classification. More specifically, for this classifier, the modulation kurtosis is estimated, compared to the true values of the modulation kurtosis for all possible modulation schemes, and the nearest modulation kurtosis value is chosen. For this figure, the modulation schemes considered were BPSK,

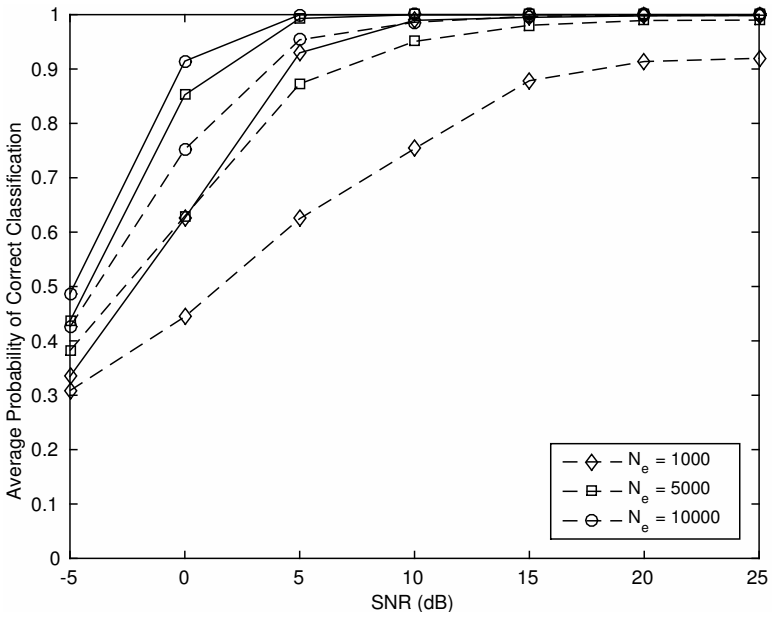

Figure 3.5: Average probability of correct classification of the proposed asynchronous feature-based classifier as a function of the number of observed symbols N_e. The performance of the optimal likelihood-based classifier is included for comparison [16].

QPSK, 16-QAM, and 64-QAM. Additionally, this feature-based classifier is compared to the performance of the optimal likelihood-based classifier, in which synchronization and known channel parameters is assumed, given in [16].

A couple of observations can be made from this figure. First, the performance of this feature-based classifier improves as the SNR and/or the number of observed symbols, N_e, increases. Secondly, the performance of the classifier approaches that of the optimal likelihood-based classifier as the number of observed symbols increases.

3.3.5 Over-The-Air Experimental Results

This section describes an over-the-air experiment to analyze the performance of the developed modulation kurtosis estimator in a realistic sensing scenario. Fig. 3.6 presents a block diagram that outlines the signal flow from the transmitter to the receiver given an AWGN transmit channel. Both the transmitter and receiver were implemented as flowgraphs in GNURadio Companion using prebuilt signal processing blocks, as well as a developed modulation kurtosis estimator block.

The hardware configuration for the two USRPs in this block diagram is shown in Fig. 3.7. This hardware configuration consists of two Ettus B210 USRPs with Vert900 antennas. Additionally, each USRP is connected to an Ettus OctoClock-G to provide a GPS Disciplined Oscillator (GPSDO) to mitigate the impact of frequency and timing drift during the observation intervals. For the analysis that follows, the center frequency chosen for the signal of interest is 900 MHz (chosen given the acceptable range of the Vert900 antennas). The sample rate for the transmit and receive flowgraphs is 8MHz (within the operating range of the B210 USRPs) and the symbol rate is 533.333 kHz, therefore oversampling the signal by a factor of 15.

Fig. 3.8 presents the performance of the proposed approach to modulation kurtosis estimation from simulation (solid lines) as well as from over-the-air experimentation (dashed lines) for a QPSK modulated signal transmitted in an AWGN channel. For these results, the NMSE is again used in order to quantify the estimator's performance. For each data

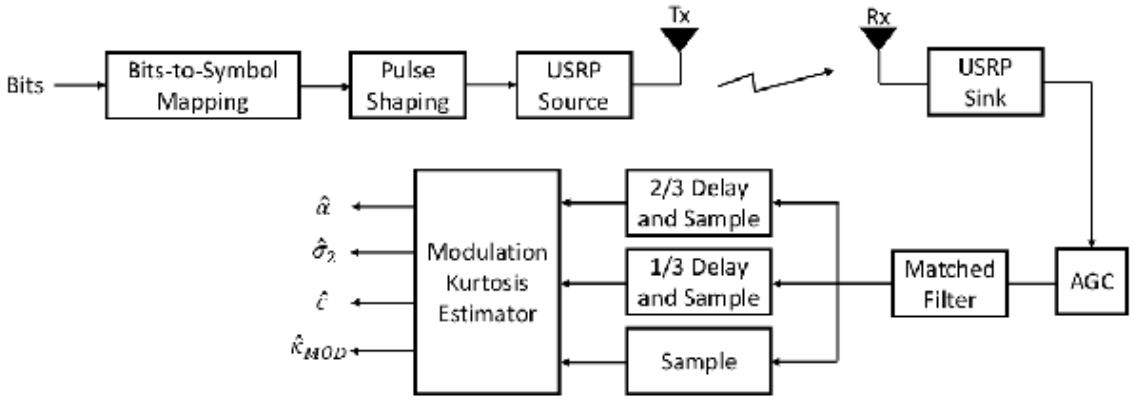

Figure 3.6: Block diagram of the over-the-air experiment.

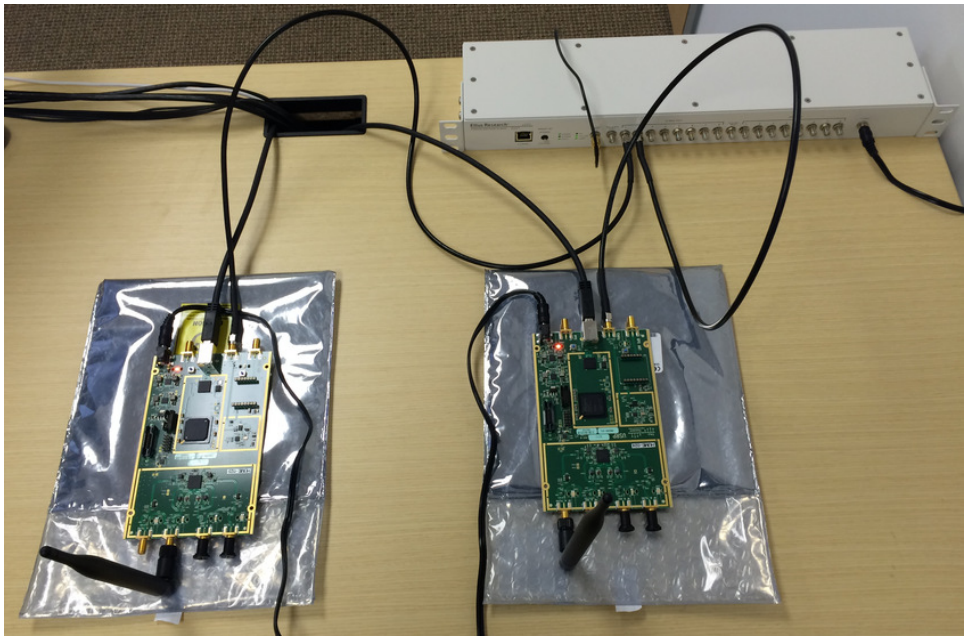

Figure 3.7: The hardware setup for the over-the-air experiment. The transmitter (left) and receiver (right) are both B210 USRPs with Vert900 antennas. An Ettus Octoclock-G is used to minimize the frequency and timing drift experienced during observation periods.

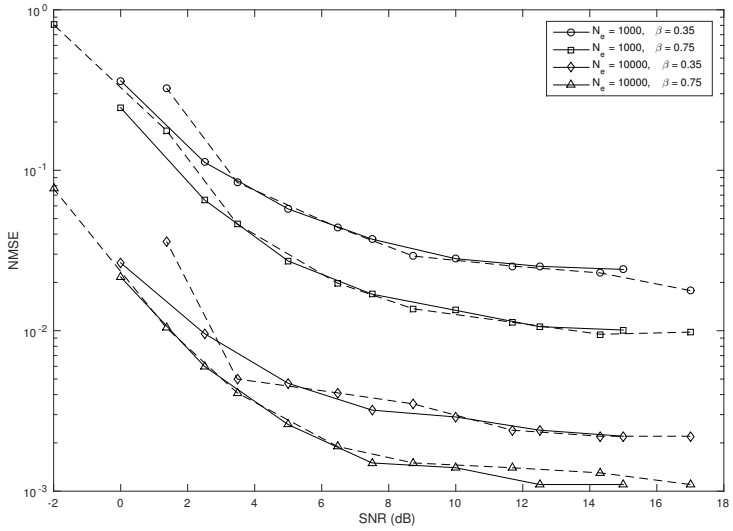

Figure 3.8: NMSE of the proposed modulation kurtosis estimator obtained through GNURadio simulation (solid lines) and through over-the-air experimentation (dashed lines) for varying N_e and β given a QPSK modulated signal received in an AWGN channel.

point on the plots, the set of λ values $\{0, 1/3, 2/3\}$ are used for estimating the unknown channel and timing parameters and the fractional time delay is swept across its range of 0 to 1 during the performance calculations through the use of a delay block in the receiver flowgraph. Finally, the SNR values for the experimental data points are determined by using the gain and noise variance estimates of the developed method-of-moments based estimator:

$$\text{SNR} = 10\log_{10}\left(\frac{\hat{\alpha}^2}{\hat{\sigma}^2}\right) \tag{3.10}$$

A few important observations can be made from this figure. First, as was discussed in Section 3.3.4, as the SNR, roll-off factor β, and/or observation length N_e increases, the NMSE decreases as expected. Secondly, and most importantly, the experimental results (the dashed lines) match up well to the simulation results (the solid lines).

3.4 Summary

In this chapter, a novel feature-based modulation classification approach was developed for asynchronously received LDAPM signals in slowly-varying frequency-flat fading channels. First, a closed-form solution for the kurtosis for these signals was defined and was shown to be invariant to the phase of the received signal, as well as to small frequency offsets of the receiver. From the kurtosis of the received signal, an estimation approach utilizing the method-of-moments based estimator developed in the previous chapter was developed for estimating and the kurtosis of the received signal's modulation scheme. Through both simulation and experimental analysis, it was shown that this estimated kurtosis of the modulation scheme can be used in order to classify the modulation scheme of the received signal.

Chapter 4

Exploiting Sensor Correlation and Reliability Information in Collaborative Spectrum Sensing

As previously discussed in the preceding chapters, spectrum sensing performance at a given sensor is a function of the transmitted signal of interest, the wireless propagation channel, and the hardware and software capabilities of the sensor itself. In other words, wireless propagation effects such as path-loss, shadowing, and multi-path fading, as well as sensor characteristics such as its noise figure, sensing algorithm, and available sensing time, can significantly impact the sensing performance of a given sensor [13], [47]. It is due to these facts that the concept of collaborative spectrum sensing is a highly studied area of research in recent years (see [48]-[57], among many others).

As the name implies, collaborative spectrum sensing is the process of using a network of sensors in order to jointly perform spectrum sensing. The idea is that it can typically be expected that not all of the collaborative sensors will experience the same detrimental propagation effects at the same instant of time, nor will all of the sensors have the same hardware and software capabilities. That is, collaborative spectrum sensing can lead to improved sensing performance through both large scale and small scale diversity.

Prior research in collaborative spectrum sensing has demonstrated that knowledge of the wireless propagation environment and sensor position information can lead to more efficient collaborative spectrum sensing algorithms. For instance, research presented in [22] and [23] shows that the reliability of each sensor (due to fading effects or the sensor's proximity to the signal of interest's transmitter, for example) should be considered in algorithm development. Additionally, research presented in [24],[25] and [52],[53] demonstrates that the spatial correlation among the sensors' observations (which due to multi-path and/or shadowing effects is a function of sensor separation) should also be considered in algorithm development.

These prior works, among others, have separately considered the effects of sensor correlation and sensor reliability information on collaborative sensing. However, the consideration of their joint effect on collaborative spectrum sensing is at present underdeveloped. Motivated by this fact, this chapter concerns the development of a collaborative signal detection approach that utilizes both sensor position dependent correlation and sensor reliability information.

To begin this development, Section 4.2 presents a collaborative signal detection scenario

in which the collaborating sensors have differing reliabilities, due to variations in their noise powers and their distance from the signal of interest's transmitter, and correlations, due to the assumption of a shadow fading wireless propagation environment. Given this scenario, a collaborative detection algorithm that incorporates both sensor reliability and correlation information is developed in Section 4.3. Through simulation, it is demonstrated that the developed collaborative detection algorithm outperforms algorithms that consider partial, or no, information of these effects.

Finally, in Section 4.4, sensor reliability and sensor correlation information is utilized in order to facilitate intelligent sensor selection. More specifically, it is shown that sensor weightings determined from the collaborative signal detection algorithm, which are inherently a function of both the sensor reliability and correlation information, can be used to intelligently choose a subset of the total available sensors. Through simulation, it is shown that selection of a subset of the sensors in this more intelligent manner greatly outperforms random subset selection, leading to more efficient trade-offs between collaborative sensing performance and sensing overhead.

4.1 Acknowledgments

This chapter, in part, is a reprint of the material as it appears in the publication:

- W. C. Headley, V. G. Chavali, and C. R. C. M. da Silva, "Exploiting radio correlation and reliability information in collaborative spectrum sensing," in *IEEE Commun. Lett.*, vol. 15, no. 8, pp. 825-827, Aug. 2011.

The dissertation author was the primary author of the research which forms the basis of this chapter, with Dr. Gautham Chavali as a secondary author and Dr. Claudio da Silva advising. Additionally, this work was supported in part by InterDigital Communications.

4.2 The Collaborative Signal Detection Scenario

For the discussion that follows, the collaborative signal detection scenario illustrated by Fig. 4.1 is considered. In this scenario, spectrum allocated to a primary spectrum user is opportunistically accessed by a collaborative secondary user network located at a distance D_S from the primary user, but within the primary user's interference range, R_P (i.e. $D_S < R_P$). Therefore, in order for the secondary user network to access the spectrum without causing interference to the primary user, the network must first detect whether or not the primary user is currently using the spectrum. This signal detection scenario can therefore be modeled as a binary hypothesis testing problem in which the null hypothesis, $\mathcal{H}_0$, represents no primary user transmission (a so-called spectrum opportunity) and the alternative hypothesis,

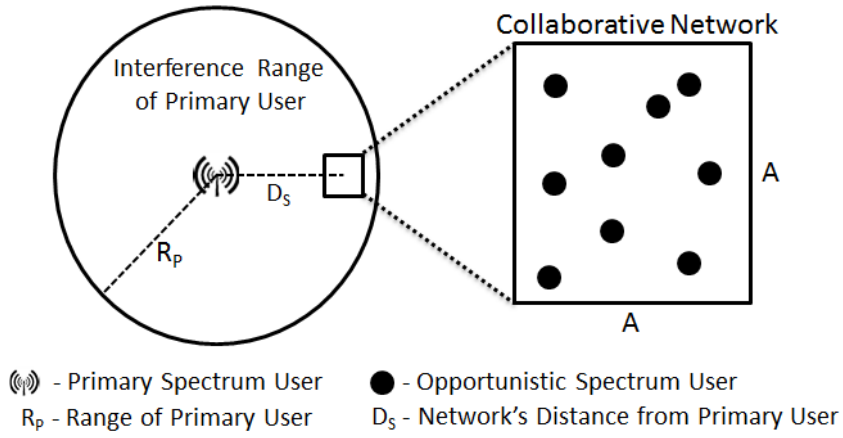

Figure 4.1: The considered collaborative signal detection scenario.

$\mathcal{H}_1$, represents primary user transmission (no spectrum opportunity exists).

The secondary user network is assumed to consist of N users that are distributed randomly, and independently, in an AxA m^2 area. When the network is performing collaborative signal detection, each of the N secondary users (acting now as sensors) performs the following signal processing tasks:

1. Measures its total received power.

2. Normalizes the total received power measurement by subtracting its mean noise power (here assumed to be known *a priori*).

3. Relays the normalized total received power measurement, Y_i (in dB, $i = \{1, 2, ..., N\}$), to a data fusion center.

The task of the fusion center, which could be a separate entity or simply one of the N secondary users in the network, is to use the collected normalized total received power

measurements, $\mathbf{Y}_F = Y_1, Y_2, \ldots, Y_N$, to determine whether or not a spectrum opportunity currently exists (this determination to be discussed in more detail in the following section).

For the null hypothesis ($\mathcal{H}_0$), the total received power measured by each sensor is simply equivalent to the sensor's noise power, due to the absence of primary user transmission. Given that the noise power can vary among the sensors (due to thermal noise, atmospheric noise, man-made noise, etc.), the sensors' noise powers are modeled as independent log-normally distributed random variables, as described in [58],[59]. Therefore, the sensors' total received power measurements Y_i, given $\mathcal{H}_0$, are independent and identically distributed Gaussian random variables with zero mean (after normalization) and known variance σ_n^2. Therefore, at the fusion center,

$$\mathcal{H}_0 \colon \mathbf{Y}_F \sim \mathcal{N}(0, \sigma_n^2 \mathbf{I}), \tag{4.1}$$

where $\mathcal{N}(0, \sigma_n^2 \mathbf{I})$ represents a zero-mean multivariate Gaussian distribution with correlation matrix $\sigma_n^2 \mathbf{I}$.

For the alternative hypothesis ($\mathcal{H}_1$), the total received power measured by each sensor is the sum of the sensor's noise power and the primary user's received signal power. Given the assumption that some of the sensors may be impacted by shadowing, experimental results have shown that the primary user's received signal power at each sensor can be approximated by a set of correlated log-normally distributed random variables, in which the mean is a function of path-loss and the variance, σ_s^2, is an experimentally obtained parameter that is dependent on the propagation environment [60]. More specifically, the primary user's signal

power received at a sensor located d meters from the primary user is given by (in dB)

$$P(d) = P_T - \bar{P}_L(d_o) - 10n \log\left(\frac{d}{d_o}\right) + \mathcal{N}(0, \sigma_s^2) \tag{4.2}$$

where P_T is the primary user's transmit power, $\bar{P}_L(d_o)$ is the average path-loss at a reference distance d_o, n is the path-loss coefficient, and $\mathcal{N}(0, \sigma_s^2)$ represents a zero-mean Gaussian random variable with variance σ_s^2. In order to model the correlation between the primary user's received signal powers at the sensors, we assume the well-known exponential model given by Gudmundson in [61]. This model defines the correlation among the sensors as

$$\rho_{i,j} = e^{-ad_{i,j}}, \tag{4.3}$$

where $d_{i,j}$ is the separation (in meters) between the i-th and j-th sensors and a is the so-called "shadowing coefficient". From [61], $a \approx 0.12$ for urban areas at 1700 MHz and $a \approx 0.002$ for suburban areas at 900 MHz, for example. (It is important to note that the collaborative signal detection algorithm to be developed in the following section is not dependent on the choice of correlation model.)

Given this definition for the primary user's received signal power, the total received power measurement at each sensor, under the alternative hypothesis, is equal to the sum of two independent log-normally distributed random variables. Various studies have shown that the sum of two independent log-normal random variables can be approximated as a log-normal random variable [62]-[64]. Using this approximation, at the fusion center

$$\mathcal{H}_1 \colon \mathbf{Y}_F \sim \mathcal{N}(\mathbf{M}, \mathbf{\Sigma}) \tag{4.4}$$

where $\mathcal{N}(\mathbf{M}, \mathbf{\Sigma})$ represents a multivariate Gaussian distribution with mean $\mathbf{M}$ and covariance matrix $\mathbf{\Sigma}$. Here, the i^{th} element of the 1xN vector $\mathbf{M}$ is given by

$$M_i = \mathrm{E}\left[10\log_{10}\left(1+\mathrm{SNR}_i\right)\right] \tag{4.5}$$

and the $\{i, j\}$ element of the NxN matrix $\mathbf{\Sigma}$ is given by

$$\sum_{i,j} = \mathrm{COV}\left(Y_i, Y_j\right) = \sigma_i \sigma_j e^{-ad_{i,j}}, \tag{4.6}$$

where σ_i^2 and σ_j^2 are the variances of measurements Y_i and Y_j, under $\mathcal{H}_1$, respectively [59].

To summarize, the fusion center's observation is defined under each hypothesis as (in dB)

$$\mathcal{H}_0 \colon \mathbf{Y}_F \sim \mathcal{N}(0, \sigma_n^2 \mathbf{I}), \tag{4.7}$$

$$\mathcal{H}_1 \colon \mathbf{Y}_F \sim \mathcal{N}(\mathbf{M}, \mathbf{\Sigma}) \tag{4.8}$$

where the i^{th} element of $\mathbf{M}$ is given by (4.5) and the $\{i, j\}$ element of $\mathbf{\Sigma}$ is given by (4.6).

4.3 The Collaborative Detection Algorithm

As defined in Section 4.2, each of the sensors in the collaborative network sends their normalized total received power measurements to a data fusion center (for this analysis, uncorrupted transmission between the sensors and the fusion center is assumed). Given that the fusion center's observation is a multivariate Gaussian distribution under both hypotheses, as defined by (4.7) and (4.8), the likelihood ratio test for the collaborative detection scenario is given by

$$\frac{\frac{1}{(2\pi)^{N/2}|\mathbf{\Sigma_1}|^{1/2}} e^{-\frac{1}{2}(\mathbf{Y}_F - \mathbf{M}_1)' \mathbf{\Sigma_1}^{-1} (\mathbf{Y}_F - \mathbf{M}_1)}}{\frac{1}{(2\pi)^{N/2}|\mathbf{\Sigma_0}|^{1/2}} e^{-\frac{1}{2}(\mathbf{Y}_F - \mathbf{M}_0)' \mathbf{\Sigma_0}^{-1} (\mathbf{Y}_F - \mathbf{M}_0)}} \underset{\mathbf{H}_0}{\overset{\mathbf{H}_1}{\gtrless}} \phi, \tag{4.9}$$

where the vector $\mathbf{M}_i$ represents the means, and the matrix $\mathbf{\Sigma}_i$ represents the covariances, of the measurements given hypothesis $\mathcal{H}_i$. Given that the measurements Y_i are independent zero-mean Gaussian random variables under $\mathcal{H}_0$, through algebraic manipulation (4.9) can be simplified as follows:

$$\begin{aligned}
\frac{|\mathbf{\Sigma_0}|^{1/2}}{|\mathbf{\Sigma_1}|^{1/2}} e^{-\frac{1}{2}(\mathbf{Y}_F-\mathbf{M}_1)'\mathbf{\Sigma_1}^{-1}(\mathbf{Y}_F-\mathbf{M}_1)+\frac{1}{2}(\mathbf{Y}_F-\mathbf{M}_0)'\mathbf{\Sigma_0}^{-1}(\mathbf{Y}_F-\mathbf{M}_0)} &\underset{\mathbf{H}_0}{\overset{\mathbf{H}_1}{\gtrless}} \phi \\
-(\mathbf{Y}_F-\mathbf{M}_1)'\mathbf{\Sigma_1}^{-1}(\mathbf{Y}_F-\mathbf{M}_1)+\mathbf{Y}_F'\mathbf{\Sigma_0}^{-1}\mathbf{Y}_F &\underset{\mathbf{H}_0}{\overset{\mathbf{H}_1}{\gtrless}} 2\ln\left(\frac{|\mathbf{\Sigma_1}|^{1/2}}{|\mathbf{\Sigma_0}|^{1/2}}\phi\right) \\
\sum_{i=1}^{N} u_i Y_i^2 - \sum_{\substack{i=1 \\ i\neq j}}^{N}\sum_{j=1}^{N} v_{i,j} Y_i Y_j + \sum_{i=1}^{N} w_i Y_i &\underset{\mathbf{H}_0}{\overset{\mathbf{H}_1}{\gtrless}} \phi^{'},
\end{aligned} \tag{4.10}$$

where

$$u_i = \frac{1}{\sigma_n^2} - Z_{i,i}^{(1)}, \quad v_{i,j} = Z_{i,j}^{(1)}, \quad w_i = 2\sum_{j=1}^{N} Z_{i,j}^{(1)} M_j^{(1)}, \tag{4.11}$$

$Z_{i,j}^{(k)}$ is the $\{i,j\}^{\text{th}}$ element of $\mathbf{\Sigma}_k^{-1}$, and $M_j^{(k)}$ is the j-th element of $\mathbf{M}_k$, given $\mathcal{H}_k$.

From (4.10), it can be observed that the developed collaborative detection algorithm for the considered collaborative spectrum sensing scenario is a non-linear weighted function of each sensor's total received power measurement. Most importantly, the weights u_i, $v_{i,j}$, and w_i, given by (4.11), are a function of both the means and covariances of the total received power measurements under $\mathcal{H}_1$. In other words, the weighting of a given sensor is inherently a function of both the statistical reliability of the measurements at the sensor (due to its proximity to the primary user and its noise power) and how correlated its measurements are with the other sensors' measurements (due to shadowing effects).

4.3.1 Simulation Results

Figs. 4.2-4.4 present simulation results of the performance of the developed collaborative signal detection algorithm given by (4.10). For these results, the receiver operating characteristic (ROC) is used in order to quantify the algorithm's performance. That is, these figures show the average probability of spectrum opportunity detection (i.e. the probability of *correctly* determining that the primary user is *not* transmitting) as a function of the probability of false opportunity (i.e. the probability of *incorrectly* determining that the primary user is *not* transmitting). Additionally, for these figures the following simulation parameters are used: $\sigma_n = 1$, $\sigma_s = 2.5$, and $a = 0.2$.

Fig. 4.2 presents ROC curves for two types of collaborative detection algorithms. The first detection algorithm is an ignorant algorithm that assumes that all of the sensors are independent (that is, $\sum_{i,j} = 0$ for $i \neq j$) and have the same reliability (that is, M_i and σ_i are equal for all sensors). The second detection algorithm is the developed algorithm given by (4.10).

A few important observations can be made from this figure. First, it can be seen that the developed algorithm which utilizes correlation and reliability information greatly outperforms the ignorant algorithm, as expected. Secondly, the performance of the algorithms improves as the number of sensors increases. It is worth noting that when the distribution of the fusion center's observations is given by (4.7) and (4.8), the developed algorithm's performance always improves as N increases. However, this is not true for the ignorant algorithm.

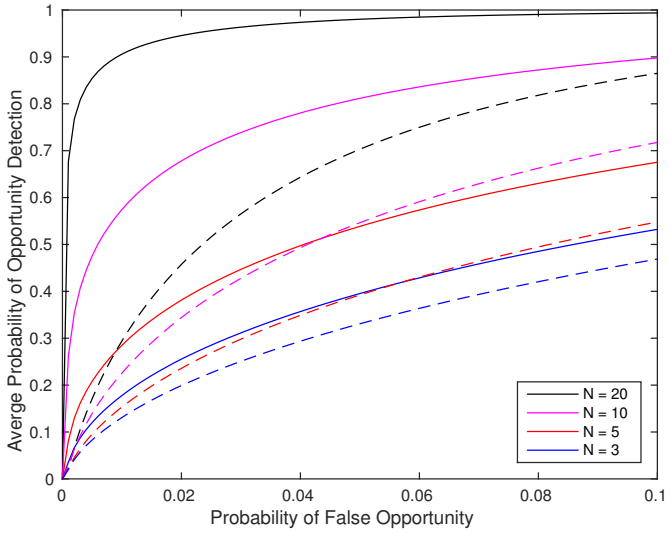

Figure 4.2: ROC curves given different numbers of collaborating sensors N and $A = 30$m (solid: the developed detection algorithm, dashed: a detection algorithm ignorant to sensor reliability and correlation information).

Figs. 4.3 and 4.4 present ROC curves for four types of collaborative detection algorithms:

- D_1 - an ignorant algorithm in which the sensors are assumed to be independent and have the same reliability
- D_2 - an algorithm in which the sensor's reliabilities are known but the sensors are assumed to be independent
- D_3 - an algorithm in which the sensors' correlations are known but the sensor's reliabilities are assumed to be the same
- D_4 - the developed algorithm given by (4.10).

In Fig. 4.3, the ROC curves of these algorithms are presented given a propagation envi-

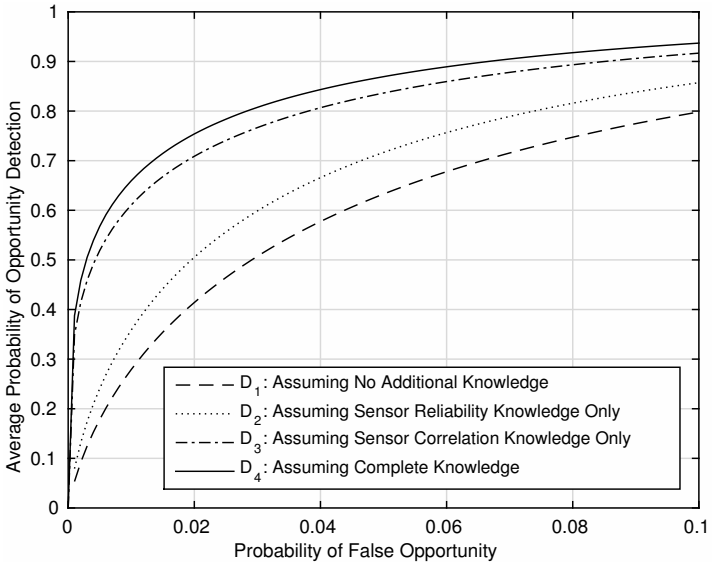

Figure 4.3: ROC curves for a few collaborative signal detection algorithms given a sensor correlation dominated environment, $A = 25$m, and $N = 10$.

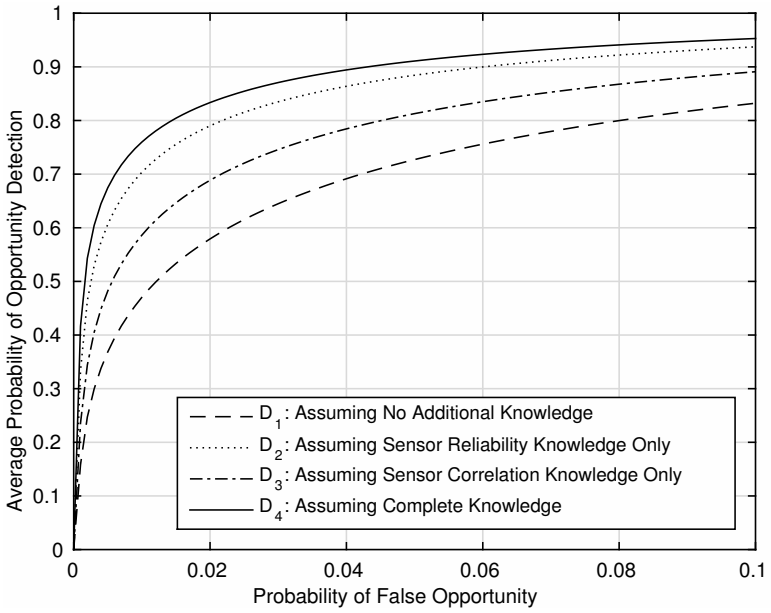

Figure 4.4: ROC curves for a few collaborative signal detection algorithms given a sensor reliability dominated environment, $A = 50$m, $N = 10$.

ronment in which the impact of sensor correlation information is greater than that of sensor reliability information. For this environment, the proposed algorithm D_4 and algorithm D_3 outperform algorithms D_1 and D_2, as expected. Conversely, Fig. 4.4 presents the ROC curves of these algorithms given a propagation environment in which the impact of sensor reliability information is greater than that of sensor correlation information. For this environment, the proposed algorithm D_4 and algorithm D_2 outperform algorithms D_1 and D_3. As expected, for both environments the developed algorithm, which utilizes both the correlation and reliability information, outperforms all other considered algorithms.

4.4 Intelligent Sensor Selection based on Correlation and Reliability Information

It was demonstrated in the previous section that the reliability of each sensor, as well as how correlated each sensor is with one another, can have a significant impact on the performance of collaborative signal detection. More specifically, it was observed from the developed collaborative detection algorithm, given by (4.10), that sensors with a low reliability and/or are correlated heavily with the other sensors have smaller weights than sensors that are more reliable and/or are less correlated with the other sensors. To better highlight this fact, the

collaborative signal detection algorithm given by (4.10) can be rewritten as:

$$\begin{aligned}
\sum_{i=1}^{N} u_i Y_i^2 - \sum_{\substack{i=1 \\ i\neq j}}^{N}\sum_{j=1}^{N} v_{i,j} Y_i Y_j + \sum_{i=1}^{N} w_i Y_i \underset{\mathbf{H}_0}{\overset{\mathbf{H}_1}{\gtrless}} \phi' \\
\sum_{i=1}^{N} Y_i^2 - \sigma_n^2 \sum_{i=1}^{N} Y_i \left\{ \sum_{j=1}^{N} Z_{i,j}^{(1)} \left(Y_j - 2M_j^{(1)} \right) \right\} \underset{\mathbf{H}_0}{\overset{\mathbf{H}_1}{\gtrless}} \phi'' \\
\sum_{i=1}^{N} Y_i^2 - \sum_{i=1}^{N} x_i Y_i \underset{\mathbf{H}_0}{\overset{\mathbf{H}_1}{\gtrless}} \phi''
\end{aligned} \tag{4.12}$$

where

$$x_i = \sigma_n^2 \sum_{j=1}^{N} Z_{i,j}^{(1)} \left(Y_j - 2M_j^{(1)} \right). \tag{4.13}$$

Rewriting the developed collaborative detection algorithm in this way leads to a single weighting for each of the collaborative sensors, given by (4.13). These weights are a function of the sensors' reliabilities, their correlations, and their instantaneous total received power measurements.

In collaborative spectrum sensing, there is an inherent trade-off between the number of collaborating sensors and the sensing overhead required [65]. In other words, as the number of collaborating sensors increases, so does the communication times, bandwidth requirements, and power needs of the sensing network. In order to attempt to strike a balance between collaborative sensing performance and overhead, intelligent sensor selection can be used.

As the name implies, intelligent sensor selection is the process of utilizing prior knowledge of each sensor's capabilities in order to determine a suitable subset of the total number of sensors for collaborative sensing. In prior works, it was shown that knowledge of the sensor's reliabilities [54] and correlations [55]-[57] can be used to facilitate intelligent sensor selection.

However, the joint consideration of both reliability and correlation information was not considered.

With this in mind, the following approach to intelligent sensor selection, that makes use of both sensor reliability and correlation information, is developed for the considered collaborative signal detection scenario:

1. Determine the average values for the sensor weights given by (4.13).
2. Find the sensor with the lowest average weight and remove it from the sensor set.
3. Recalculate the weights for the new subset of sensors.
4. Repeat Steps 1-3 until the desired performance bound or number of sensors is reached.

4.4.1 Simulation Results

Fig. 4.5 presents simulation results of the performance of the developed intelligent sensor selection algorithm. More specifically, in this figure, ROC curves are used in order to quantify the performance of the intelligent sensor selection algorithm against that of random sensor selection, given the following simulation parameters: $N = 15$, $A = 50$, $\sigma_n = 1$, $\sigma_s = 2.5$, and $a = 0.2$. From this figure, it can be observed that the developed intelligent sensor selection algorithm, that utilizes both the sensor reliability and sensor correlation information, outperforms four cases of random sensor selection, in which this information is not considered. It should be noted that, on average, the developed intelligent sensor selection algorithm outperforms random sensor selection, as expected.

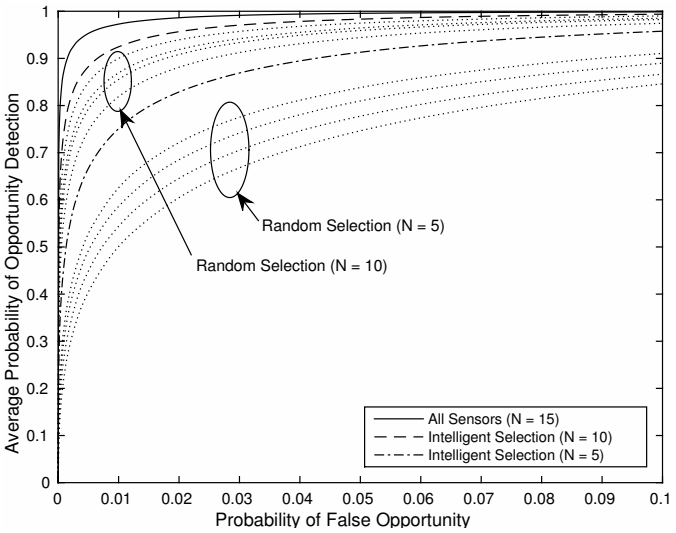

Figure 4.5: ROC curves of the developed collaborative signal detection algorithm given intelligent sensor selection and random sensor selection.

4.5 Summary

In this chapter, the impact of sensor reliability and sensor correlation information on collaborative signal detection was considered. First, a novel collaborative signal detection algorithm was developed that utilizes both sensor reliability and sensor correlation information. Through simulation, this algorithm was shown to outperform algorithms in which partial, or none, of this information is considered. Secondly, this chapter demonstrated that sensor reliability and correlation information can also be utilized in order to perform more intelligent sensor selection. Through simulation, it was shown that the developed intelligent sensor selection algorithm on average has a much lower impact on the detector's performance than random sensor selection.

Chapter 5

Conclusions

The work presented in this dissertation has advanced the state-of-the-art in spectrum sensing research by relaxing some of the common signal, channel, and Tx/Rx impairment assumptions that have been typically considered in the literature. Making valid assumptions on available *a priori* knowledge for the given spectrum sensing application is a critical consideration in the development of any spectrum sensing technique. For example, in opportunistic spectrum sharing and military applications, which have been the two main thrusts for spectrum sensing research in recent years, it can inherently be expected that limited, or no, *a priori* knowledge of the signal of interest will be available. Given this fact, the research presented in this dissertation has taken a major step closer to the ultimate goal of spectrum sensing research in these applications, that of performing fast and reliable spectrum sensing with no assumed prior knowledge of the signal of interest. The contributions of this dissertation are as follows.

The work presented in Chapters 2 and 3 concerns the development of both a novel signal and channel parameter estimator, as well as a novel classifier of the modulation scheme, for any generic linear digital amplitude-phase modulated signal (such as PAM, PSK, QAM, etc.) transmitted through a slowly-varying frequency-flat fading channel. In the development of these sensing techniques, the common assumption of a known channel model (complete or partial knowledge of the received signal gain, signal phase, time delay, and noise variance induced by the channel) and the assumption that the transmitter and receiver are synchronized in time and frequency are relaxed. As previously stated, the relaxation of these common assumptions is critically important for sensing scenarios in which the signal source is uncooperative, given that typically assumed channel equalization and synchronization aids such as training sequences or *a priori* known signal parameters may be incomplete or unavailable.

More specifically, in Chapter 2, first a closed-form signal and channel parameter estimation approach based upon the method-of-moments is developed for estimating the received signal gain, noise variance, and fractional timing offset of the received signal. Here, previously undefined closed-form equations for the 2^{nd} absolute moments required by the estimator are derived for a root-raised cosine pulse shape and are shown to require no *a priori* knowledge of the signal phase or modulation scheme of the received signal. Simulation results demonstrate that the developed estimator outperforms the traditional synchronous method-of-moments estimator for the received signal gain and noise variance, colloquially known as the M_2M_4 estimator, when the transmitter and receiver are asynchronous and the modulation format is unknown. Finally, Chapter 2 also presents the development of a novel quasi-Hybrid like-

lihood ratio test based modulation classifier that utilizes the developed signal and channel parameter estimator to classify the modulation format of the received signal.

While the performance of the developed asynchronous likelihood-based modulation classifier is shown to approach that of the optimal synchronous likelihood-based classifier given an adequate observation interval, it requires perfect knowledge, or estimates, of the carrier frequency and phase of the received signal. In order to relax these requirements, Chapter 3 extends the work of Chapter 2 by presenting a novel feature-based modulation classifier in which the statistical measure of kurtosis is utilized as the modulation discriminating feature of the received signal. To begin the development of this classifier, first a previously undefined closed-form equation for the kurtosis of the received signal of interest is derived and is shown to be a function of the kurtosis of the modulation scheme of the transmitted signal. Additionally, it is shown that the derived kurtosis equation ignores phase information and is immune to reasonable frequency offsets between the transmitter and receiver.

From this closed-form kurtosis equation, and given the signal and channel parameter estimator developed in Chapter 2, an estimation and classification technique is developed to determine the modulation scheme of the received signal from the kurtosis. The performance of this technique is analyzed first through simulation and is shown to perform comparatively to the developed likelihood-based classifier, and greatly outperforms this classifier given frequency offsets or unknown phase information. Secondly, an over-the-air experimental setup is developed and used to demonstrate that the theoretical and simulation results match well with the results gathered through experimentation.

While Chapters 2 and 3 advance the state-of-the-art in the area of single user spectrum sensing, the aim of the work presented in Chapter 4 is to advance the state of the art in the area of collaborative spectrum sensing. More specifically, this chapter considers the joint impact of sensor correlation and reliability information in the development of collaborative signal detection and intelligent sensor selection algorithms. Prior works have typically discussed the impact of sensor correlation and reliability information independent of one another and thus only address a subset of the potential collaborative spectrum sensing scenarios that can arise. For instance, correlation among the collaborating sensors can be expected in shadowing and/or multi-path fading environments. Additionally, deep fades, shadowing, and/or the sensors having more sophisticated sensing algorithms or more time to devote to sensing can lead to the sensors having different reliabilities.

With these thoughts in mind, Chapter 4 develops a collaborative signal detection algorithm that makes use of both sensor correlation and reliability information for an outlined realistic collaborative sensing scenario. Through simulation, it is shown that the developed algorithm outperforms algorithms that consider partial, or none, of this information. Next, given the developed algorithm, an approach to intelligent sensor selection (i.e. choosing a subset of the total number of sensors for collaboration) is developed that leverages both the correlation and reliability information. Simulation results show that intelligently choosing a subset of the sensors with this approach greatly outperforms random sensor selection.

Appendix A

Derivation of Closed-Form Equations for $\psi^{(2)}_{\lambda,\epsilon}$ and $\psi^{(4)}_{\lambda,\epsilon}$

Closed-form equations for $\psi^{(2)}_{\lambda,\epsilon}$ and $\psi^{(4)}_{\lambda,\epsilon}$, defined generally by (2.9), can be determined through the use of the Poisson Summation Formula given by [66]

$$\sum_{k=-\infty}^{\infty} x(t+kT) = \frac{1}{T}\sum_{k=-\infty}^{\infty} X\left(\frac{k}{T}\right) e^{j2\pi(\frac{k}{T})t}, \tag{A.1}$$

where $X(\cdot)$ is the Fourier transform of the function $x(\cdot)$. Here, closed-form equations are developed for a root-raised cosine pulse shaping function with roll-off factor β. However, this approach can be applied equivalently for other pulse shaping functions of interest.

1.1 Derivation of $\psi^{(2)}_{\lambda,\epsilon}$

Substituting (2.9), with $a = 2$, into (A.1) leads to

$$\psi^{(2)}_{\lambda,\epsilon} = \sum_{k'=-\infty}^{\infty} R((\lambda-\epsilon)T + k'T)^2 = \frac{1}{T}\sum_{k'=-\infty}^{\infty} \tilde{R}^{(2)}\left(\frac{k'}{T}\right) e^{j2\pi k'(\lambda-\epsilon)}, \tag{A.2}$$

where $\tilde{R}^{(2)}(\cdot)$ is the Fourier transform of $R(\cdot)^2$. For the root-raised-cosine pulse shape, $\tilde{R}(\cdot)$ is by definition the raised-cosine pulse shape, which has a frequency-domain representation that is given by [37]

$$\tilde{R}(f) = \begin{cases} T, & |f| \leq \frac{1-\beta}{2T} \\ \frac{T}{2}\left[1+\cos\left(\frac{\pi T}{\beta}[|f|-\frac{1-\beta}{2T}]\right)\right], & \frac{1-\beta}{2T} < |f| \leq \frac{1+\beta}{2T} \\ 0, & \text{otherwise} \end{cases} \tag{A.3}$$

Therefore, $\tilde{R}^{(2)}$ can be determined by convolving this equation with itself. The resulting equation is non-zero only within the range $[-(1+\beta)/T,(1+\beta)/T]$, leading to the following simplification for (A.2):

$$\begin{aligned} \psi^{(2)}_{\lambda,\epsilon} &= \frac{1}{T}\sum_{k'=-1}^{1} \tilde{R}^{(2)}\left(\frac{k'}{T}\right) e^{j2\pi k'(\lambda-\epsilon)} \\ &= \tilde{R}^{(2)}\left(-\frac{1}{T}\right) e^{-j2\pi(\lambda-\epsilon)} + \tilde{R}^{(2)}(0) + \tilde{R}^{(2)}\left(\frac{1}{T}\right) e^{j2\pi(\lambda-\epsilon)} \\ &= \frac{1}{T}\left(\frac{\beta T}{8} e^{-j2\pi(\lambda-\epsilon)} + \left(T - \frac{\beta T}{4}\right) + \frac{\beta T}{8} e^{j2\pi(\lambda-\epsilon)}\right) \\ &= 1 + \frac{\beta}{4}\left(\cos\left(2\pi(\lambda-\epsilon)\right) - 1\right). \end{aligned} \tag{A.4}$$

1.2 Derivation of $\psi^{(4)}_{\lambda,\epsilon}$

Substituting (2.9), with $a = 4$, into (A.1) leads to

$$\sum_{k'=-\infty}^{\infty} R((\lambda-\epsilon)T + k'T)^4 = \frac{1}{T}\sum_{k'=-\infty}^{\infty} \tilde{R}^{(4)}\left(\frac{k'}{T}\right) e^{j2\pi k'(\lambda-\epsilon)}, \tag{A.5}$$

where $\tilde{R}^{(4)}(\cdot)$ is the Fourier transform of $R(\cdot)^4$. As before, using the fact that multiplication in the time-domain is equivalent to convolution in the frequency-domain, $\tilde{R}^{(4)}(\cdot)$ is equivalent

to the term $\tilde{R}^{(2)}(\cdot)$ convolved with itself. Solving for this convolution, $\tilde{R}^{(4)}(\cdot)$ is found to be non-zero only in the range $[-(2+2\beta)/T,(2+2\beta)/T]$, leading to the following simplification for (A.5):

For $\beta \geq 0.5$,

$$
\begin{aligned}
\psi^{(4)}_{\lambda,\epsilon} \;=\; & \Bigg[\frac{(2\beta^3(4\pi^2-123)+3\beta^2(41-4\pi^2)+6\pi^2\beta-\pi^2)\cos(\frac{\pi}{\beta})}{384\pi^2} \\
& +\frac{3\beta(\beta^2(8\pi^2-35)-8\pi^2\beta+2\pi^2)\sin(\frac{\pi}{\beta})}{128\pi^3} \\
& +\frac{8\beta^3(\pi^2-6)+12\beta^2(2-\pi^2)+6\pi^2\beta-\pi^2}{48\pi^2}\Bigg]\cos(6\pi(\lambda-\epsilon)) \\
& -\Bigg[\frac{(2\beta^3(4\pi^2-123)+3\beta^2(41-4\pi^2)+6\pi^2\beta-\pi^2)\cos(\frac{\pi}{\beta})}{96\pi^2} \\
& +\frac{3\beta(\beta^2(8\pi^2-35)-8\pi^2\beta+2\pi^2)\sin(\frac{\pi}{\beta})}{32\pi^3} \\
& +\frac{3\beta^3(26\pi^2-105)+192\beta^2(2-\pi^2)+96\pi^2\beta-16\pi^2}{192\pi^2}\Bigg]\cos(4\pi(\lambda-\epsilon)) \\
& +\Bigg[\frac{3\beta(\beta^2(2\pi^2+55)-2\pi^2\beta-6\pi^2)\sin(\frac{2\pi}{\beta})}{2048\pi^3} \\
& +\frac{(7(2\beta^3(4\pi^2-123)+3\beta^2(41-4\pi^2)+6\pi^2\beta-\pi^2)\cos(\frac{\pi}{\beta})}{384\pi^2} \\
& -\frac{3\beta(\beta^2(2\pi^2+55)-2\pi^2\beta-6\pi^2)\cos(\frac{\pi}{\beta})\sin(\frac{\pi}{\beta})}{1024\pi^3}+\frac{21\beta(\beta^2(8\pi^2-35)-8\pi^2\beta+2\pi^2)\sin(\frac{\pi}{\beta})}{128\pi^3} \\
& +\frac{\beta^3(2\pi^2+39)-12\beta^2(\pi^2+6)+14\pi^2\beta+3\pi^2}{16\pi^2}\Bigg]\cos(2\pi(\lambda-\epsilon)) \\
& +\frac{\beta(\beta^2(2\pi^2-11)+3\pi^2\beta+\pi^2)\sin(\frac{\pi}{\beta})}{1024\pi^3}-\frac{\beta(\beta^2(2\pi^2-11)+3\pi^2\beta+\pi^2)\cos(\frac{\pi}{\beta})\sin(\frac{\pi}{\beta})}{512\pi^3} \\
& -\frac{(2\beta^3(4\pi^2-123)+3\beta^2(41-4\pi^2)+6\pi^2\beta-\pi^2)\cos(\frac{\pi}{\beta})}{96\pi^2} \\
& -\frac{3\beta(\beta^2(8\pi^2-35)-8\pi^2\beta+2\pi^2)\sin(\frac{\pi}{\beta})}{32\pi^3} \\
& +\frac{\beta^3(22\pi^2-591)+1152\beta^2-96\pi^2\beta+144\pi^2}{192\pi^2}
\end{aligned}
\tag{A.6}
$$

For $\beta \leq 0.5$,

$$\begin{aligned}\psi^{(4)}_{\lambda,\epsilon} &= \beta^3 \frac{50\pi^2 - 453}{192\pi^2} \left(\cos(4\pi(\lambda-\epsilon)) - 4\cos(2\pi(\lambda-\epsilon)) + 3\right) \\ &\quad -\beta^2 \frac{8-\pi^2}{\pi^2} \left(\cos(2\pi(\lambda-\epsilon)) - 1\right) \\ &\quad + \frac{\cos(2\pi(\lambda-\epsilon)) + 2}{3}\end{aligned} \tag{A.7}$$

1.3 Impact of Pulse Shape Truncation on $\psi^{(2)}_{\lambda,\epsilon}$ and $\psi^{(4)}_{\lambda,\epsilon}$

In reality, pulse shaping functions do not have infinite time support and thus are truncated to some finite time length. This truncation can lead to measurable differences between what is observed in practice and the theoretical values of $\psi^{(2)}_{\lambda,\epsilon}$ and $\psi^{(4)}_{\lambda,\epsilon}$ just developed. Figs. A.1-A.4 present simulation results of the mean absolute percentage error (MAPE) of these values as a function of the time support N_T, the roll-off factor β, and the fractional time delay ϵ (here, $\lambda = 0$ without loss of generality). For this analysis, the time support of the root-raised cosine pulse is defined as a span of N_T symbols.

As can be observed from these figures, as the time support N_T increases, the MAPE reduces, as expected. Additionally, from Figs. A.1 and A.2, it can be observed that the MAPE decreases as the roll-off factor β increases. This makes sense given that, as the name implies, the pulse shaping function decays quicker for higher roll-off factors. Finally, from Figs. A.3 and A.4, it can be observed that the MAPE decreases as the fractional time delay ϵ decreases.

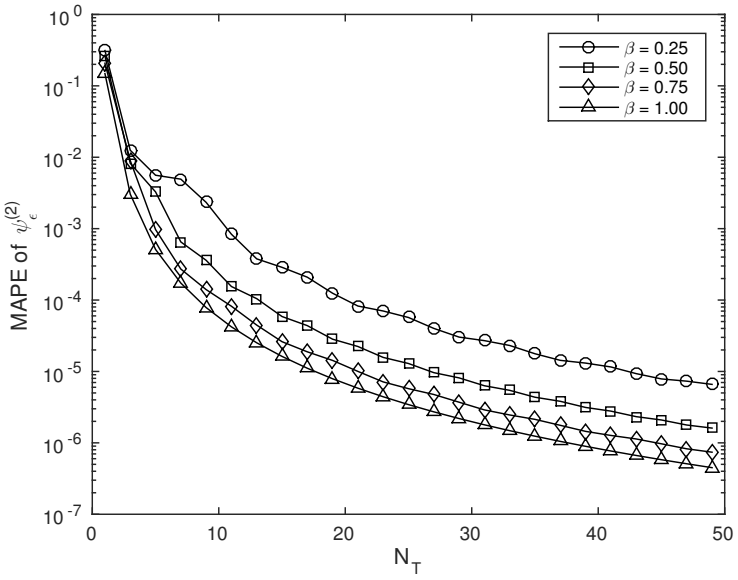

Figure A.1: Mean absolute percentage error of $\psi_\epsilon^{(2)}$ as a function of the time support N_T and differing values of the roll-off factor β (averaged over the fractional time delay ϵ).

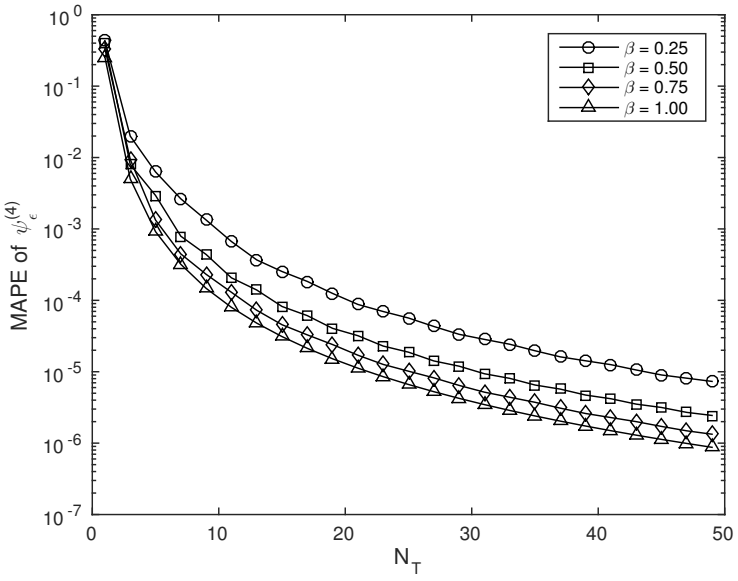

Figure A.2: Mean absolute percentage error of $\psi_\epsilon^{(4)}$ as a function of the time support N_T and differing values of the roll-off factor β (averaged over the fractional time delay ϵ).

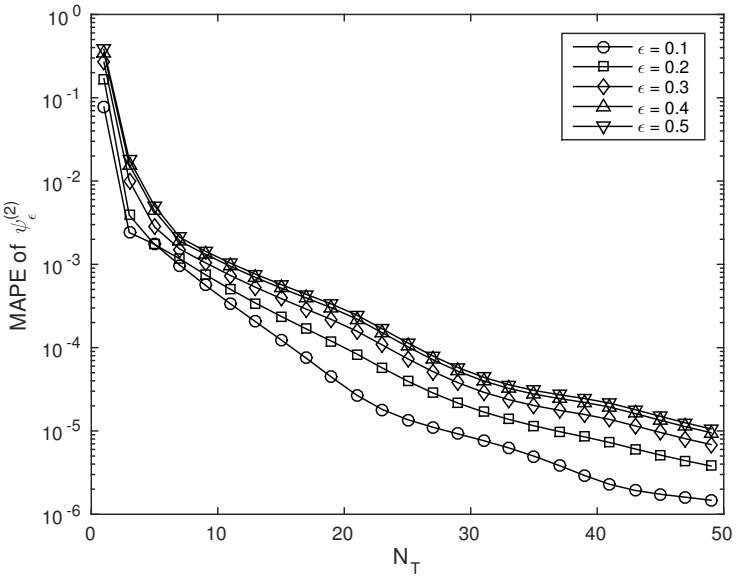

Figure A.3: Mean absolute percentage error of $\psi_\epsilon^{(2)}$ as a function of the time support N_T and differing values of the fractional time delay ϵ (averaged over the roll-off factor β).

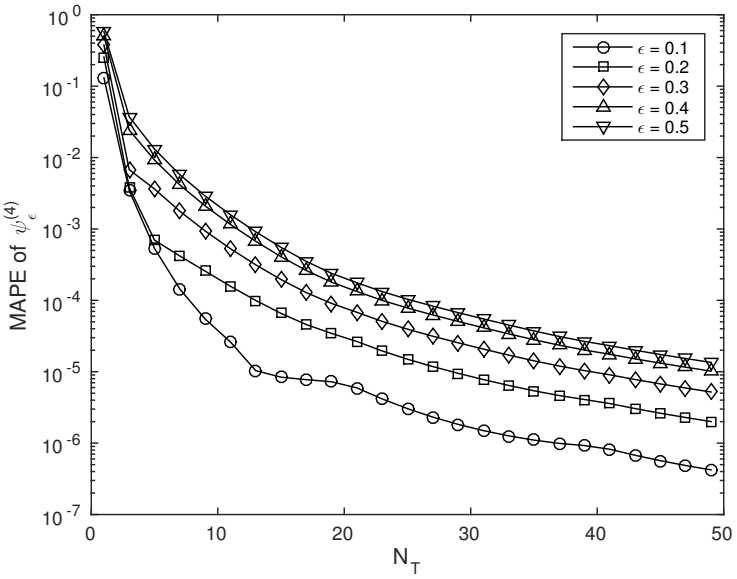

Figure A.4: Mean absolute percentage error of $\psi_\epsilon^{(4)}$ as a function of the time support N_T and differing values of the fractional time delay ϵ (averaged over the roll-off factor β).

Appendix B

Derivation of the Asynchronous Kurtosis

From (3.1), the kurtosis of the complex-valued asynchronously received symbols given by (2.5) can be written as

$$\kappa_r = \frac{\mathrm{E}[|r_{m,\lambda}|^4] - 2\mathrm{E}[|r_{m,\lambda}|^2]^2 - |\mathrm{E}[r_{m,\lambda}^2]|^2}{\mathrm{E}[|r_{m,\lambda}|^2]^2}, \tag{B.1}$$

where from (2.8),

$$\mathrm{E}[|r_{m,\lambda}|^2] = \alpha^2 \psi_{\lambda,\epsilon}^{(2)} + 4\sigma^2. \tag{B.2}$$

The remaining terms of (B.1) are developed in a similar fashion to yield

$$\begin{aligned}
\mathrm{E}[r_{m,\lambda}^2] &= \mathrm{E}\left[\left(\alpha e^{j\theta} \sum_{k'=-\infty}^{\infty} S_{m-l-k'} R((k'+\lambda-\epsilon)T) + n_m\right)^2\right] \\
&= \mathrm{E}\left[\left(\alpha e^{j\theta} \sum_{k'=-\infty}^{\infty} S_{m-l-k'} R((k'+\lambda-\epsilon)T)\right)^2\right] + \mathrm{E}\left[n_m^2\right] \\
&= \alpha^2 \mathrm{E}[s_{\Re}^2] \psi_{\lambda,\epsilon}^{(2)} - \alpha^2 \mathrm{E}[s_{\Im}^2] \psi_{\lambda,\epsilon}^{(2)}
\end{aligned} \tag{B.3}$$

and

$$\begin{aligned}
\mathrm{E}[|r_{m,\lambda}|^4] &= \mathrm{E}\left[\left|\alpha e^{j\theta}\sum_{k'=-\infty}^{\infty} S_{m-l-k'}R((k'+\lambda-\epsilon)T)+n_m\right|^4\right] \\
&= \mathrm{E}\left[\left|\alpha e^{j\theta}\sum_{k'=-\infty}^{\infty} S_{m-l-k'}R((k'+\lambda-\epsilon)T)\right|^4\right] \\
&\quad +16\sigma^2\mathrm{E}\left[\left|\alpha e^{j\theta}\sum_{k'=-\infty}^{\infty} S_{m-l-k'}R((k'+\lambda-\epsilon)T)\right|^2\right]+\mathrm{E}\left[|n_m|^4\right] \\
&= \alpha^4\left(\mathrm{E}[s_{\Re}^4]+\mathrm{E}[s_{\Im}^4]+2\mathrm{E}[s_{\Re}^2 s_{\Im}^2]\right)\psi_{\lambda,\epsilon}^{(4)}+16\alpha^2\sigma^2\psi_{\lambda,\epsilon}^{(2)}+32\sigma^4 \\
&\quad +\alpha^4\left(3\mathrm{E}[s_{\Re}^2]^2+3\mathrm{E}[s_{\Im}^2]^2+2\mathrm{E}[s_{\Re}^2]\mathrm{E}[s_{\Im}^2]\right)(\psi_{\lambda,\epsilon}^{(2)^2}-\psi_{\lambda,\epsilon}^{(4)}),
\end{aligned} \tag{B.4}$$

where $\psi_{\lambda,\epsilon}^{(2)}$ and $\psi_{\lambda,\epsilon}^{(4)}$ are derived in Appendix A and $s_{\Re}$ and $s_{\Im}$ denote the real and imaginary components of the random modulated data symbols given by (3.2). Note that these terms are independent of the integer symbol offset values m and l given independent and uniformly chosen modulated data symbols.

Finally, plugging these three terms into (B.1) and performing some algebraic manipulation:

$$\kappa_r = \kappa_{\mathrm{MOD}}\frac{\alpha^4\psi_{\lambda,\epsilon}^{(4)}}{(\alpha^2\psi_{\lambda,\epsilon}^{(2)}+4\sigma^2)^2}, \tag{B.5}$$

where κ_{MOD} is the *modulation kurtosis* defined by (3.3).

Bibliography

[1] T. Yucek and H. Arslan, "A survey of spectrum sensing algorithms for cognitive radio applications," in *IEEE Commun. Surveys and Tuts.*, vol. 11, no. 1, pp. 116-130, March 2009.

[2] President's Council of Advisors on Science and Technology (PCAST), "Report to the president: realizing the full potential of government-held spectrum to spur economic growth," July 2012 [Online]. Available: https://www.whitehouse.gov/administration/eop/ostp/pcast/docsreports.

[3] European Parliament and Council, "Decision no. 243/2012/EU of the European parliament and of the council of 14 March 2012 establishing a multiannual radio spectrum policy programme," March 2012 [Online]. Available: http://eur-lex.europa.eu/legal-content/EN/TXT/?uri=CELEX:32012D0243.

[4] Shared Spectrum Company, "Spectrum occupancy measurements," [Online]. Available: http://www.sharedspectrum.com/papers/spectrum-reports.

[5] K. Patil, R. Prasad, and K. Skouby, "A survey of worldwide spectrum occupancy measurement campaigns for cognitive radio," in *Proc. IEEE ICDeCom*, Feb. 2011, pp. 1-5.

[6] FCC Spectrum Policy Task Force, "Report of the spectrum efficiency working group," Nov. 2002 [Online]. Available: http://www.fcc.gov/sptf/reports.html.

[7] S. M. Dudley, W. C. Headley, M. Lichtman, E. Y. Imana, X. Ma, M. Abdelbar, A. Padaki, A. Ullah, M. M. Sohul, T. Yang, and J. H. Reed, "Practical issues for spectrum management with cognitive radios," in *Proc. of the IEEE*, vol. 102, no. 3, pp. 242-264, March 2014.

[8] C. Santivanez, R. Ramanathan, C. Partridge, R. Krishnan, M. Condell, and S. Polit, "Opportunistic spectrum access: challenges, architecture, protocols," in *Proc. ACM WICON*, Aug. 2006.

[9] I. F. Akyildiz, L. Won-Yeol, C. Mehmet, and S. Mohanty, "A survey on spectrum management in cognitive radio networks," in *IEEE Commun. Mag.*, vol. 46, no. 4, pp. 40-48, April 2008.

[10] J. M. Park, J. H. Reed, A. A. Beex, T. C. Clancy, V. Kumar, and B. Bahrak, "Security and enforcement in spectrum sensing," in *Proc. of the IEEE*, vol. 102, no. 3, pp. 270-281, March 2014.

[11] O. Fatemieh, A. Farhadi, R. Chandra, and C. Gunter, "Using classification to protect the integrity of spectrum measurements in white space networks," in *Proc. Netw. and Dist. System Security Symp.*, Feb. 2010.

[12] N. Reisi, M. Ahmadian, and S. Salari, "Performance analysis of energy detection-based spectrum sensing over fading channels," in *Proc. WiCOM*, Sept. 2010, pp. 1-4.

[13] D. Cabric, S. M. Mishra, and R. W. Brodersen, "Implementation issues in spectrum sensing for cognitive radios," in *Proc. Asilomar Conf. Signals, Syst. and Comput.*, Nov. 2004, pp. 772-776.

[14] M. Oner and O. Dobre, "On the second-order cyclic statistics of signals in the presence of receiver impairments," in *IEEE Tran. Commun.*, vol. 59, no. 12, pp. 3278-3284, Dec. 2011.

[15] J. Verlant-Chenet, J. Renard, J. M. Dricot, P. De Doncker, and F. Horlin, "Sensitivity of spectrum sensing techniques to RF impairments," in *Proc. VTC*, May 2010, pp. 1-5.

[16] W. Wei and J. M. Mendel, "Maximum-likelihood classification for digital amplitude-phase modulations," in *IEEE Trans. Commun.,* vol. 48, no 2, pp. 189-1983, Feb. 2000.

[17] J. L. Xu, W. Su, and M. Zhou, "Software-defined radio equipped with rapid modulation recognition," in *IEEE Trans. Veh. Tech.*, vol. 59, no. 4, pp. 1659-1667, May 2010.

[18] J. A. Sills, "Maximum-likelihood modulation classification for PSK/QAM," in *Proc. IEEE Military Commun. Conf.*, Nov. 1999, pp. 57-61.

[19] P. Panagiotou, A. Anastasoupoulos, and A. Polydoros, "Likelihood ratio tests for modulation classification," in *Proc. IEEE Military Commun. Conf.*, Oct. 2000, pp. 670-674.

[20] O. A. Dobre and F. Hameed, "Likelihood-based algorithms for linear digital modulation classification in fading channels," in *Proc. IEEE Canadian Conf. Electr. Comp. Eng.*, May 2006, pp. 1347-1350.

[21] F. Hameed, O. A. Dobre, and D. Popescu, "On the likelihood-based approach to modulation classification," in *IEEE Trans. Wireless Commun.*, vol. 8, no. 12, pp. 5884-5892, Dec. 2009.

[22] F. E. Visser, G. J. M. Janssen, and P. Pawelczak, "Multinode spectrum sensing based on energy detection for dynamic spectrum access," in *Proc. IEEE Veh. Tech. Conf.*, May 2008, pp.1394-1398.

[23] J. Ma, G. Zhao, and Y. Li, "Soft combination and detection for cooperative spectrum sensing in cognitive radio networks," in *IEEE Trans. Wireless Commun.*, vol. 7, no. 11, pp. 4502-4507, Nov. 2008.

[24] E. Visotsky, S. Kuffner, and R. Peterson, "On collaborative detection of TV transmissions in support of dynamic spectrum sharing," in *Proc. IEEE Dynamic Spectrum Access Netws.*, Nov. 2005, pp. 338-345.

[25] A. Ghasemi and E. S. Sousa, "Asymptotic performance of collaborative spectrum sensing under correlated log-normal shading," in *IEEE Commun. Lett.*, vol. 11, no. 1, pp. 34-36, Jan. 2007.

[26] S. M. Kay, *Fundamentals of Statistical Signal Processing*. Prentice Hall, 1998, vol. I.

[27] F. W. Smith and M. H. Wright, "Automatic ship photo interpretation by the method of moments," in *IEEE Trans. on Comp.*, vol. C-20, no. 9, pp. 1089-1095, Sept. 1971.

[28] H. R. M. S. Jalali and H. Ghoddusi, "Estimation of unknown parameters in systems dynamics models using the method of simulated moments," in *Proc. Winter Sim. Conf.*, Dec. 2013, pp. 1212-1222.

[29] O. Dobre, A. Abdi, Y. Bar-Ness, and W. Su, "A survey of automatic modulation classification techniques: classical approaches and new trends," in *Proc. IET Commun.*, vol. 1, no. 2, April 2007, pp. 137-156.

[30] M. Lichtman, W. C. Headley, and J. H. Reed, "Automatic modulation classification under IQ imbalance using supervised learning," in *Proc. IEEE MILCOM*, Nov. 2013, pp. 1622-1627.

[31] W. Dan, G. Xuemai, and G. Qing, "A new scheme of automatic modulation classification using wavelet and WSVM," in *Proc. Int. Conf. on Mobile Tech., Apps., and Systs.*, Nov. 2005, pp. 5-9.

[32] W. C. Headley, J. D. Reed, and C. R. C. M. da Silva, "Distributed cyclic spectrum feature-based modulation classification," in *Proc. IEEE WCNC*, March 2008, pp. 1200-1204.

[33] S. M. Kay, *Fundamentals of Statistical Signal Processing*. Prentice Hall, 1998, vol. II.

[34] H. L. Van Trees, *Detection, Estimation, and Modulation Theory*. Wiley, 2001, vol. 1.

[35] U. Mengali and A. N. D'Andrea, *Synchronization Techniques for Digital Receivers*. Plenum Press, 1997.

[36] C. N. Georghiades, "Blind carrier phase acquisition for QAM constellations," in *IEEE Trans. Commun.*, vol. 45, no. 11, pp. 1477-1486, Nov. 1997.

[37] J. G. Proakis and M. Salehi, *Digital Communications*. McGraw Hill, 2008.

[38] R. Dwyer, "Use of the kurtosis statistic in the frequency domain as an aid in detecting random signals." *IEEE Journal of Oceanic Eng.*, vol. 9, no. 2, pp. 85-92, April 1984.

[39] O. Shalvi and E. Weinstein, "New criteria for blind deconvolution of nonminimum phase systems (channels)," *IEEE Trans. Info. Theory*, vol. 36, no. 2, pp. 312-321, March 1990.

[40] R. De Roo, S. Misra, and C. Ruf, "Sensitivity of the kurtosis statistic as a detector of pulsed sinusoidal RFI," in *IEEE Trans. on Geoscience and Remote Sens.*, vol. 45, no. 7, pg. 1938-1946, July 2007.

[41] J. Zhang, J. Salmi, and E. Lohan, "Analysis of kurtosis-based LOS/NLOS identification using indoor MIMO channel measurement," in *IEEE Trans. on Veh. Tech.*, vol. 62, no. 6, pp. 2871-2874, July 2013.

[42] J. Gunther and T. Moon, "Burst mode synchronization of QPSK on AWGN channels using kurtosis," in *IEEE Trans. Commun.*, vol. 75, no. 8, pp. 2453-2462, Aug. 2009.

[43] A. Subekti and A. Suksmono, "Kurtosis-based spectrum sensing for cognitive wireless cloud computing network," in *Proc. ICCCSN*, April 2012, pp. 26-27.

[44] K. Davidson, J. Goldschneider, L. Cazzanti, and J. Pitton, "Feature-based modulation classification using circular statistics," in *Proc. MILCOM*, Nov. 2004, pp. 765-771.

[45] H. Mathis, "On the kurtosis of digitally modulation signals with timing offsets," in *Proc. IEEE SPAWC*, March 2001, pp. 86-89.

[46] E. Zervas, J. Proakis, and V. Eyuboglu, "Effects of constellation shaping on blind equalization," in *Proc. SPIE*, Dec. 1991, pp. 178-187.

[47] N. S. Shankar, C. Cordeiro, and K. Challapali, "Spectrum agile radios: utilization and sensing architectures," in *Proc. IEEE Dynamic Spectrum Access Netws.*, Nov. 2005, pp.160-169.

[48] I. F. Akyildiz, B. F. Lo, and R. Balakrishnan, "Cooperative spectrum sensing in cognitive radio networks: a survey," in *Physical Commun. Journal*, vol. 4, no. 1, pp. 40-72, March 2011.

[49] A. Ghasemi and E. S. Sousa, "Opportunistic spectrum access in fading channels through collaborative sensing," *Journal of Commun.*, vol. 2, no. 2, pp. 71-82, March 2007.

[50] M. Velempini, V. Moyo, and M. E. Dlodlo, "Improving local and collaborative spectrum sensing in cognitive networks through the implementation of cognitive collaborators," in *Proc. IEEE MELECON*, March 2012, pp. 1045-1048.

[51] A. Singh, M. R. Bhatnagar, and R. K. Mallik, "Cooperative spectrum sensing in multiple antenna based cognitive radio network using an improved energy detector," in *IEEE Commun. Lett.*, vol. 16, no. 1, pp. 64-67, Jan. 2012.

[52] K. Arshad and K. Moessner, "Optimization of collaborative spectrum sensing with SIMO cognitive terminals using genetic algorithm," in *Proc. IEEE Int. Symp. on Pers., Indoor, and Mobile Radio Commun.*," Sept. 2009, pp. 1707-1711.

[53] J. Zhou, Y. Shen, and Y. Tang, "Optimal antenna location of secondary user for spectrum sensing in cognitive radio networks," in *IEEE Commun. Lett.*, vol. 17, no. 9, pp. 1746-1749, Sept. 2013.

[54] R. Tandon, B. Dey, and S. Nandi, "Weight based clustering in wireless sensor networks," in *Proc. NCC*, Feb. 2013, pp. 15-17.

[55] Y. Selen, H. Tullberg, and J. Kronander, "Sensor selection for cooperative spectrum sensing," in *Proc. IEEE DySPAN*, Oct. 2008, pp. 14-17.

[56] D. Li, W. Zou, Z. Zhou, and Y. Ye, "Sensor selection for collaborative spectrum sensing using SVD-QR," in *Proc. CHINACOM*, Aug. 2010, pp. 25-27.

[57] B. Liu, W. Mingchen, C. Zhang, and C. W. Chen, "Robust sensor selection for collaborative spectrum sensing with attacks under correlated shadowing," in *Proc. IEEE Int. Conf. on Commun. Workshops*, June 2014, pp. 279-284.

[58] K. V. Cai, V. Phan, and R. J. O'Conner, "Energy detector performance in a noise fluctuating channel," in *Proc. IEEE Military Commun. Conf.*, Oct. 1989, pp. 85-89.

[59] J. Unnikrishnan and V. V. Veeravalli, "Cooperative sensing for primary detection in cognitive radio," *IEEE J. Sel. Topics Signal Process.*, vol. 2, no. 1, pp. 18-27, Feb. 2008.

[60] T. S. Rappaport, *Wireless Communications Principles and Practice*. Prentice Hall, 2002.

[61] M. Gudmendson, "Correlation model for shadow fading in mobile radio systems," in *Electon. Lett.*, vol. 27, no. 23, pp. 2145-2146, Nov. 1991.

[62] S. Schwartz and Y. Yeh "On the distribution function and moments of power sums with lognormal components," in *Bell Syst. Tech. J.*, vol. 61, no. 7, pp. 1441-1462, Sept. 1982.

[63] L. F. Fenton, "The sum of lognormal probability distributions in scatter transmissions systems," in *IRE Trans. Commun. Syst.*, vol. CS-8, no. 1, pp. 57-67, March 1960.

[64] J. Wu, N. B. Mehta, and J. Zhang, "A flexible lognormal sum approximation method," in *Proc. IEEE Global Commun. Conf.*, Dec. 2005, pp. 3413-3417.

[65] W. S. Jeon, D. H. Lee, and D. G. Jeong, "Collaborative sensing management for cognitive radio networks with reporting overhead," in *IEEE Trans. on Commun.*, vol. 12, no. 2, pp. 595-605, Feb. 2013.

[66] D. Zwillinger, *CRC Standard Mathematical Tables and Formulae*. CRC Press, 2003.